



Mapping protein dynamics at high spatial resolution with temperature-jump X-ray crystallography

Received: 16 November 2022

Accepted: 17 August 2023

Published online: 18 September 2023

Check for updates

Alexander M. Wolff^{ID 1}, Eriko Nango^{ID 2,3}✉, Iris D. Young^{4,5}, Aaron S. Brewster^{ID 5}, Minoru Kubo^{ID 2,6}, Takashi Nomura^{2,6}, Michihiro Sugahara², Shigeki Owada², Benjamin A. Barad^{ID 4,17}, Kazutaka Ito^{ID 7}, Asmit Bhowmick^{ID 5}, Sergio Carbajo^{ID 8,9}, Tomoya Hino^{10,11}, James M. Holton^{ID 5,12,13}, Dohyun Im¹⁴, Lee J. O'Riordan⁵, Tomoyuki Tanaka^{2,14}, Rie Tanaka^{ID 2,14}, Raymond G. Sierra^{ID 8}, Fumiaki Yumoto^{15,18}, Kensuke Tono^{ID 2,16}, So Iwata^{ID 2,14}, Nicholas K. Sauter^{ID 5}, James S. Fraser^{ID 4} & Michael C. Thompson^{ID 1}✉

Understanding and controlling protein motion at atomic resolution is a hallmark challenge for structural biologists and protein engineers because conformational dynamics are essential for complex functions such as enzyme catalysis and allosteric regulation. Time-resolved crystallography offers a window into protein motions, yet without a universal perturbation to initiate conformational changes the method has been limited in scope. Here we couple a solvent-based temperature jump with time-resolved crystallography to visualize structural motions in lysozyme, a dynamic enzyme. We observed widespread atomic vibrations on the nanosecond timescale, which evolve on the submillisecond timescale into localized structural fluctuations that are coupled to the active site. An orthogonal perturbation to the enzyme, inhibitor binding, altered these dynamics by blocking key motions that allow energy to dissipate from vibrations into functional movements linked to the catalytic cycle. Because temperature jump is a universal method for perturbing molecular motion, the method demonstrated here is broadly applicable for studying protein dynamics.

Conformational dynamics drive ubiquitous protein functions, such as enzyme catalysis, signal transduction and allosteric regulation¹. The study of protein motions is critical to our mechanistic understanding of these fundamental biological phenomena, and the ability to rationally control protein motions is a frontier for protein engineers who seek to design biomolecules with increasingly complex functions. Nevertheless, accurately modelling protein motions with atomic resolution remains a longstanding challenge for the field of structural biology². This challenge arises because data from imaging techniques such as X-ray crystallography and cryogenic

electron microscopy are inherently ensemble-averaged over space and time³. Thus, information about spatiotemporal coupling between observed alternate conformations is lost, and intermediate states that are only transiently populated at equilibrium remain invisible. For this reason, high-resolution structural information is often combined with spectroscopic measurements. Despite the power of such integrative approaches, it can be difficult to correlate spectroscopic observables with specific features of molecular structures. Time-resolved X-ray crystallography (TRX) overcomes these challenges by obtaining high-resolution information in both the spatial and

A full list of affiliations appears at the end of the paper. ✉ e-mail: eriko.nango.c4@tohoku.ac.jp; mthompson30@ucmerced.edu

temporal domains^{4–6}. In this pump–probe technique, a rapid perturbation drives molecules out of conformational equilibrium, then structural snapshots are captured as the ensemble relaxes to a new equilibrium. By sampling a series of pump–probe time delays, kinetic couplings between conformers and transiently populated structural states can be observed.

TRX experiments were pioneered on photoactive proteins^{6–8} and have become more readily accessible with the advent of X-ray free-electron lasers (XFELs), brighter synchrotrons and serial crystallography^{9–11}. The scope of TRX has broadened through the use of photocaged ligands¹², rapid mix-and-inject experiments¹³ and electric-field-based perturbations⁵. Still, it remains challenging to excite a protein’s intrinsic dynamics in a generalizable manner for time-resolved structural studies. While many perturbations are tailored to the protein of interest, protein dynamics are universally coupled to thermal fluctuations of the surrounding solvent¹⁴. Recent multi-temperature-crystallography experiments demonstrated that modifying temperature allows one to tune the conformational ensemble sampled at equilibrium, paving the way for temperature-jump (T-jump) TRX experiments^{15,16}. Infra-red (IR) laser-induced T-jump are routinely used to study protein folding and enzyme dynamics^{17–19}. In such experiments, a mid-IR laser excites the O-H stretching mode of water molecules, resulting in rapid heating of the sample. Both solvent heating²⁰ and heat transfer through the protein²¹ happen on faster timescales than most functional protein motions, removing the conformational ensemble from thermal equilibrium. Subsequently, the system relaxes to a new equilibrium, determined by the final temperature, as a subset of the molecules in the sample populate higher-energy conformational states. At both temperatures, the protein exists as an ensemble of conformations. At higher temperatures, higher energy conformations will be more highly populated due to Boltzmann statistics^{3,22}. Previously, T-jump was coupled to small-angle X-ray scattering (SAXS) to perform time-resolved measurements of protein structural dynamics^{23,24}. Infra-red laser pulses have also been used to study thermal denaturation of an enzyme in crystallo, but prior work lacked rigorous time-resolved measurements of the motions induced by rapid heating²⁵.

In this Article, we present time-resolved T-jump serial femtosecond crystallography (SFX) experiments on a model system, lysozyme, demonstrating that T-jumps are an effective perturbation for measuring the intrinsic conformational dynamics of proteins. We used a nanosecond pulsed laser tuned to the mid-IR region of the electromagnetic spectrum to heat the bulk solvent within and around lysozyme microcrystals. These microcrystals were delivered to the pump–probe interaction region using a free-flowing microfluidic stream and were subsequently probed using ultrafast, high-intensity XFEL pulses (Fig. 1). We detected the introduction of a T-jump directly from singular value decomposition (SVD) of the isotropic diffuse scattering present in diffraction images, and using a repertoire of real space analysis tools including weighted difference electron density maps²⁶ and structure refinement against extrapolated structure factors^{27,28}, we revealed that the rapid heating of the crystals excites the intrinsic dynamics of crystallized lysozyme molecules. At short pump–probe time delays (20 ns), we observe the signatures of widespread atomic vibrations, which dissipate to reveal coordinated motions in functionally-relevant regions of the enzyme structure at longer pump–probe time delays (20–200 μs). Our observations are consistent with prior work to elucidate the role of conformational dynamics in lysozyme’s function. Furthermore, T-jump TRX allowed us to directly visualize the effect of an inhibitor on the observed motions of the enzyme. This work opens the door for future T-jump TRX experiments on diverse protein systems by leveraging the inextricable connection between temperature and macromolecular dynamics. This includes proteins whose activities cannot be triggered by light or rapid mixing.

Results

Instrumentation and data collection

We paired an IR laser with high-resolution SFX²⁹ in a pump–probe configuration to measure the conformational dynamics of lysozyme in real time and at atomic resolution. Leveraging instrumentation compatible with standard photoactive TRX experiments^{30,31}, we tuned the pump laser to the mid-IR range to excite the O–H stretch mode of water with a pulse duration of approximately 7 ns, resulting in a T-jump³². For SFX measurements, we embedded batch-grown lysozyme microcrystals in an 18% hydroxyethyl cellulose carrier medium³³ (Extended Data Table 1) and delivered them to the pump–probe interaction region using a viscous extrusion device³⁴ that formed a free-flowing microfluidic jet (Fig. 1). Once delivered to the interaction region, crystals were rapidly heated by the IR laser. At defined time delays following the IR heating pulse (20 ns, 20 μs and 200 μs), we probed the sample with ultrafast, high-brilliance X-ray pulses (Extended Data Table 1) from the SPring-8 Angstrom Compact Linear Accelerator (SACLA) XFEL³⁵, and measured X-ray diffraction using a custom multi-panel CCD detector³⁶. The fastest measurable time delay was 7 ns, limited by the duration of the mid-IR pump laser pulse. In each of our datasets, T-jump measurements were interleaved with two measurements in which the IR laser shutter was closed, providing internal controls (Fig. 1). We refer to the sequential interleaved dark measurements as ‘dark1’ and ‘dark2’, and these sets of interleaved control measurements were treated as separate datasets. Therefore, each of our T-jump datasets (20 ns, 20 μs and 200 μs) is paired with two internal control datasets (F_{dark1} and F_{dark2}). Additionally, a dataset was collected where the IR laser shutter remained closed (no interleaved T-jumps) which we refer to as $F_{\text{laser off}}$.

T-jump detection from diffuse scatter

During the experiment, we performed online data analysis with a computational pipeline developed specifically for data collection at SACLA³⁷, which identified, in real-time, detector images that contained X-ray diffraction from crystals and subsequently integrated and merged the growing dataset to provide preliminary feedback on data quality and dataset completeness. Following the experiment, data were processed with more rigorous optimization of parameters used for indexing and integration, as well as post-refinement during merging^{38–41}. A summary of the data quality is available (Extended Data Tables 1–3), and a detailed description of both online and offline data processing procedures are provided (Methods).

To confirm that the application of the IR pump laser introduced a T-jump in the sample, we modified tools from previous SAXS experiments²³ to analyse the scattering signal resulting from the solvent around and within the protein crystals. Starting from raw diffraction images identified as crystal hits, we azimuthally averaged the total scattering and applied a median filter to remove the effect from Bragg peaks. This generated a series of one-dimensional scattering curves that contained the isotropic signature from bulk water. These scattering curves were scaled and combined in a matrix that was analysed using SVD. SVD generated a set of right singular vectors (basis vectors) (Fig. 2a) and a set of left singular vectors that quantified the contribution of each basis vector to every scattering curve used to construct the input matrix (Fig. 2b). We observed that the contribution of the right singular vector associated with the second largest eigenvalue (v1) to each scattering image was highly correlated with whether the pump laser pulse had been applied, as determined by the distribution of entries in the corresponding left singular vector (Fig. 2c). In contrast, the contribution of other basis vectors identified by SVD (v0, v2 and v3 in Fig. 2) do not show the same dependence on the laser status. This observation provided a means to retrospectively confirm the introduction of a T-jump in all images collected under pump laser illumination by directly analysing laser-dependent changes in the background solvent scattering signal. To complement the experimental analysis, we calculated an approximate T-jump of 21 K using a

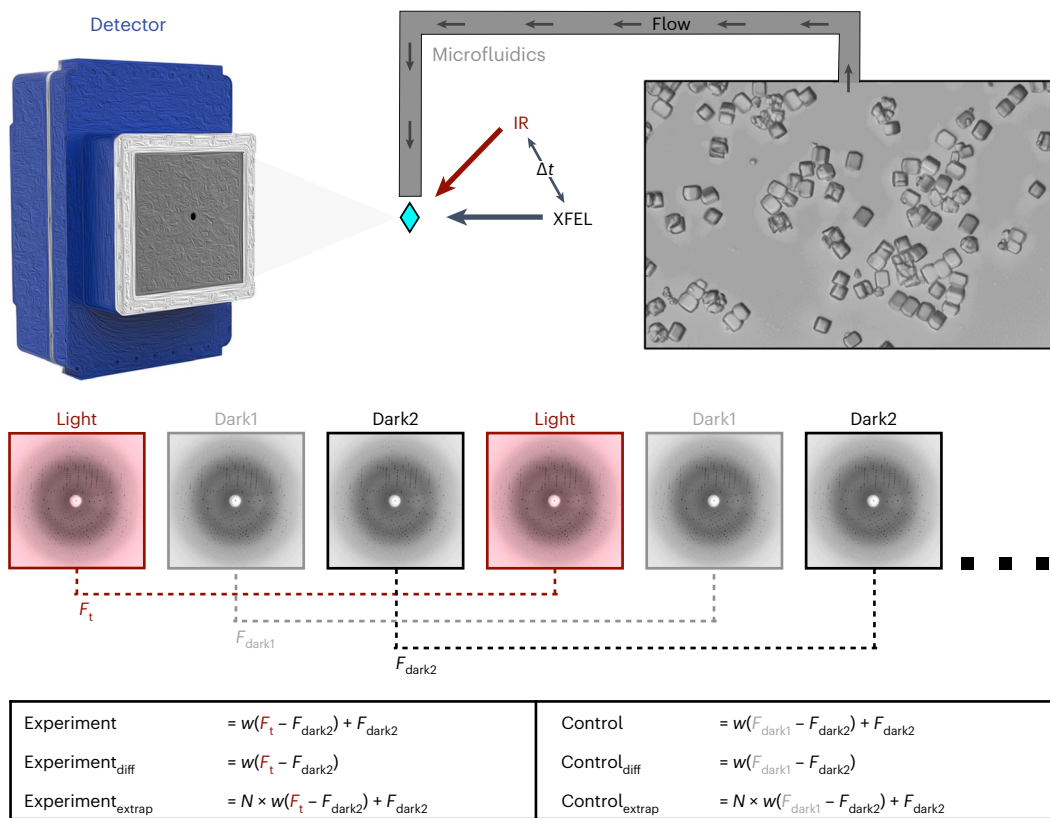


Fig. 1 | Schematic of T-jump TRX experiment. Lysozyme crystals were delivered to the pump–probe interaction region via a microfluidic jet. Light and dark images were collected in an interleaved manner, with light images defined as those where the crystal was pumped with an IR laser at a defined time delay (Δt) before being probed by the XFEL. Dark images were collected with the IR

pump shutter closed and an XFEL probe. These images were combined in post-processing to create a set of structure factors for each time delay (F_t) and as well as two corresponding sets of dark structure factors (F_{dark1} and F_{dark2}). Experiments and matching controls as defined above and in the text were analysed to identify time-dependent structural changes.

simplified model of the experiment that assumed a sample consisting of pure water (Methods).

Unit cell expansion and increased global protein dynamics

Using the processed diffraction data, we compared the unit cell dimensions as a function of pump–probe time delay. We observed that application of the IR laser results in rapid expansion of the unit cell (Fig. 2d). This thermal expansion corresponds to <1% of the length of the unit cell axes yet is statistically significant because each serial crystallography dataset contains >10,000 unique crystal measurements (Extended Data Tables 2 and 4). Furthermore, we observed that the average unit cell parameters for the interleaved F_{dark1} and F_{dark2} datasets matched the $F_{laser\ off}$ dataset much more closely than the unit cells seen in F_t datasets. This comparison suggests that the observed unit cell expansion is due to the application of the pump laser rather than variations in other parameters, such as crystal batch or sample delivery conditions. The thermal expansion of the unit cell provides further evidence of a laser-induced T-jump.

As an initial step towards identifying structural changes that were induced by a T-jump, we refined models against the F_t structure factors from each time delay. The resulting atomic coordinates were nearly identical to one another as well as to a structure refined against the $F_{laser\ off}$ data; however, we did observe an increase in the average atomic B-factor in the T-jump structures (Fig. 2e). Collectively, these observations indicate small populations of high-energy conformational states and/or motions that are well modelled by the harmonic approximation of the B-factor, especially for short (20 ns) pump–probe time delays. The models refined against the raw F_t structure factors were deposited to the Protein Data Bank (PDB).

Time-resolved electron density changes

To gain further insight into time-resolved changes in the protein structure, we created a series of difference electron density maps. These maps were created by subtracting interleaved dark2 measurements (F_{dark2}) from T-jump measurements (F_t) combined with phases from the corresponding dark state models as refined against (F_{dark2}) data. Additionally, we applied a weighting scheme developed to improve the estimation of difference structure factors calculated from noisy data²⁶. We viewed the resulting maps in the context of the corresponding dark state model and observed features consistent with time-dependent changes in the enzyme’s conformational ensemble (Fig. 3a). Generally, we observed that time-resolved difference electron density evolved from a strong ubiquitous signal centred on atom positions to coordinated positive and negative peaks that suggest correlated motions within the enzyme. Features appearing at the 20 ns time delay were widespread, with negative peaks centred on heavy atoms (non-hydrogens), surrounded by distinct positive halos (Fig. 3a, Extended Data Fig. 1a and Supplementary Video 1). In difference electron density maps corresponding to microsecond time delays (20 and 200 μ s), most difference density features manifested as coupled positive and negative peaks adjacent to the protein molecule. At 20 μ s, the largest peaks appeared at sparse locations adjacent to the backbone, indicating the beginning of coordinated motions (Fig. 3a and Supplementary Video 2). These motions continued to evolve into paired positive and negative peaks indicating coordinated shifts of the backbone away from the conformation that is most prevalent in the dark state at the 200 μ s pump–probe time delay. Residues 97–100 provide a clear example of such motions (Fig. 3a and Supplementary Video 3).

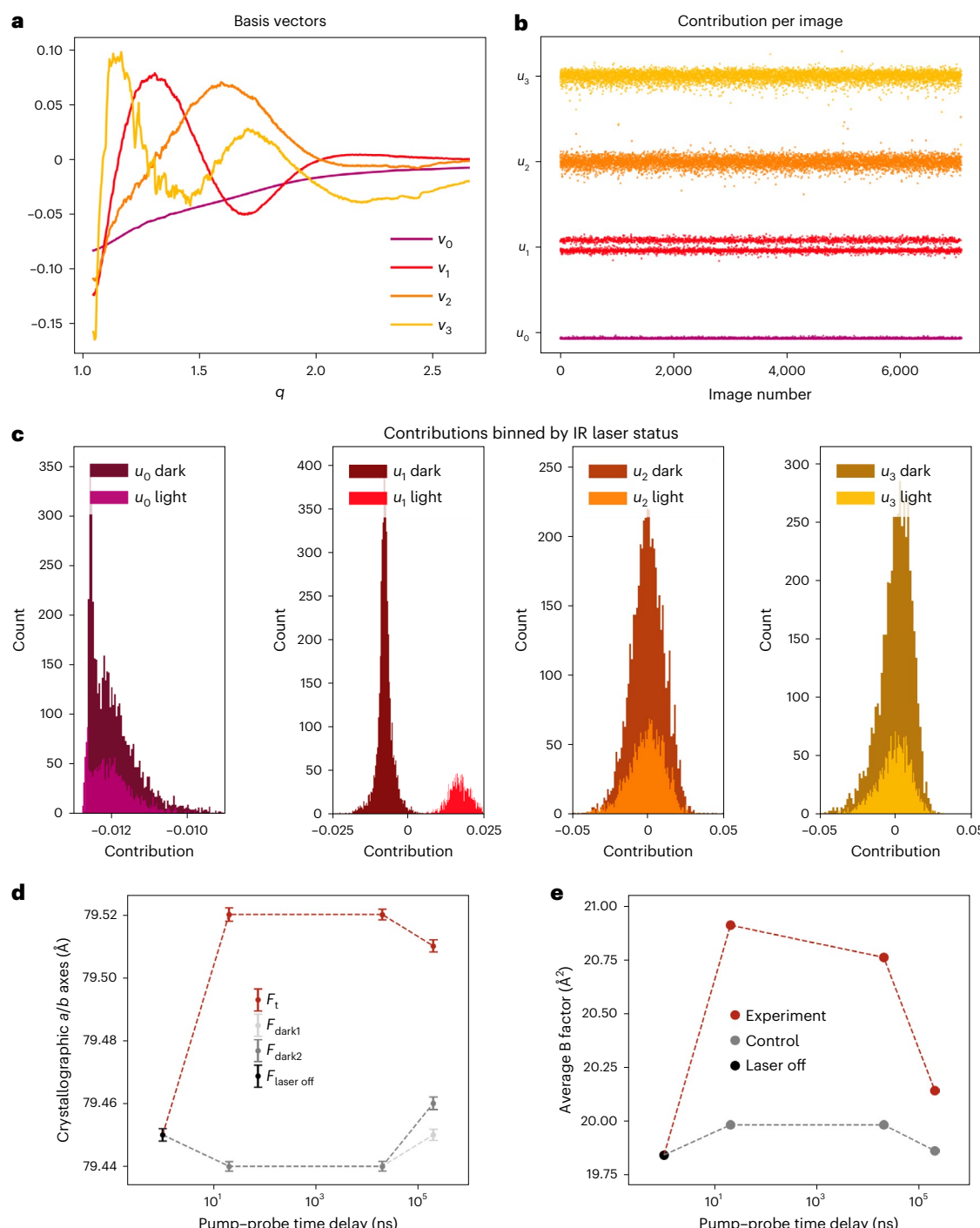


Fig. 2 | Experimental detection of T-jump. **a, b**, Radial averages of diffraction images from the 20 ns dataset were decomposed using SVD. The basis vectors (v_n) associated with the largest four singular values were visualized (a), as was the contribution (u_n) of each corresponding basis vector to each radial average (b). **c**, u_1 values were split, which was clarified by plotting the values as histograms. The values and sign of u_{in} associated with the second largest singular value, correlate with IR laser status, as reported by the IR laser diode. **d**, Analysis of the crystallographic a/b axis lengths, equivalent under $P4_32_1$ symmetry, as a function of pump–probe time delay reveal thermal expansion of the unit cell. All values in d are mean \pm 95% confidence interval. Time zero corresponds to the

laser-off (laser off; $n = 9,464$) dataset, with laser-on (light; 20 ns, $n = 15,253$; 20 μ s, $n = 13,681$; 200 μ s, $n = 11,931$) and interleaved laser-off (dark1; 20 ns, $n = 14,383$; 20 μ s, $n = 13,559$; 200 μ s, $n = 11,857$ and dark2; 20 ns, $n = 14,454$; 20 μ s, $n = 13,893$; 200 μ s, $n = 11,950$) datasets plotted for each pump–probe time delay. Unit cell dimensions expand following perturbation with an IR laser, while unilluminated data show consistent unit cell dimensions over the course of the experiment. **e**, Similarly, the average B-factor of refined models increases following perturbation with an IR laser. Models were refined against laser off, experiment or control structure factors.

To test whether the peaks observed in our difference maps were driven by the T-jump rather than experimental noise, we calculated a series of matching control difference maps using the interleaved dark datasets (F_{dark1} and F_{dark2}) (Fig. 1). Control maps contained very few

features, confirming that the signals observed in the time-resolved maps were far above the threshold of experimental noise (Extended Data Fig. 1a). To quantify this comparison, we calculated pairwise real space correlation coefficients (RSCCs) between all difference maps

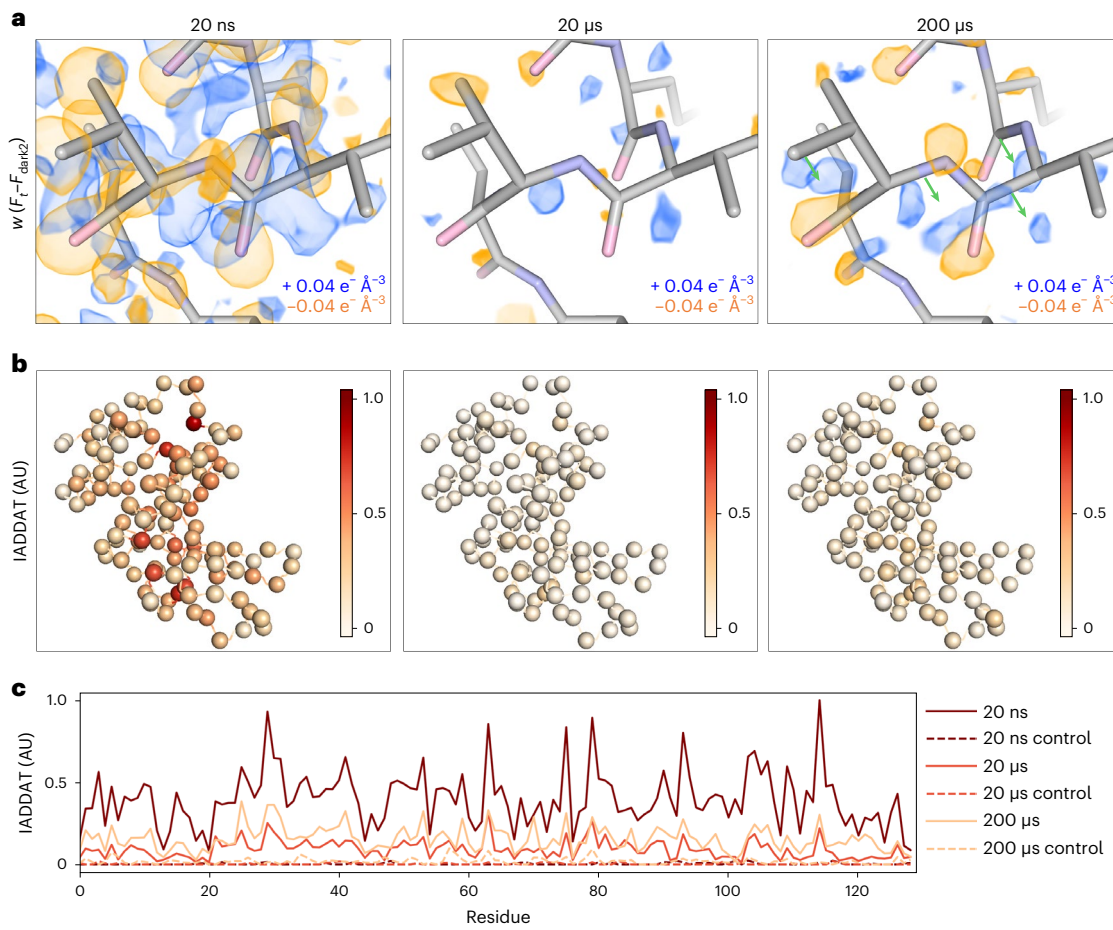


Fig. 3 | Time-resolved difference electron density evolves over time following T-jump. **a**, Comparison of weighted difference electron density maps ($F_t - F_{\text{dark}2}$) for each pump–probe time delay, centred around residues 97–100. Maps were visualized at an absolute contour level of $\pm 0.04 \text{ e}^- \text{ \AA}^{-3}$ alongside corresponding refined models. While model coordinates appeared stable across pump–probe time delays, difference maps revealed time-resolved changes to the T-jump

induced signal, with evidence for coordinated motions (green arrows) apparent by 200 μs. **b**, IADDAT was calculated as an average value per residue for each pump–probe time delay, then mapped onto C-alpha positions (spheres) of the respective model, and plotted as a function of residue number. **c**, Comparison of IADDAT values for experimental maps relative to matched controls revealed low levels of noise across the series.

(Extended Data Fig. 1b). We expected maps dominated by random noise to display no correlation, whereas systematic variations or common signals in the map would drive the RSCC towards 1. Pairwise comparisons between control maps revealed RSCC values near 0, indicating the presence of noise alone. Control maps compared with experimental maps revealed RSCC values again near 0, with a minor increase in matched pairs, indicating minor experimental variations common to the interleaved data. Finally, pairwise comparisons between experimental maps showed much larger RSCC values, ranging between 0.3 and 0.7, indicating common signals distributed over time.

To further characterize the spatial distribution of features observed in our time-resolved difference maps we integrated the absolute difference density above a noise threshold (IADDAT)^{5,42}. In this calculation, difference peaks with an absolute value greater than $0.04 \text{ e}^- \text{ \AA}^{-3}$ and within 2.5 Å of an atom (excluding waters) are summed, and an average value is calculated on a per residue basis. Then, the per residue values are scaled and mapped onto corresponding C-alpha positions (Fig. 3b). At all pump–probe time delays, the distribution of difference density is non-uniform across the molecule, indicating specific regions of enhanced dynamics (Fig. 3b). The difference density is also quantitatively strongest in the map corresponding to the 20 ns pump–probe time delay and weakest in the map corresponding to the 20 μs time delay (Fig. 3c). This spatial analysis revealed which local regions of the enzyme respond most strongly to the T-jump, as well as

the timescales of these responses. IADDAT calculations on matched control maps ($F_{\text{dark}1} - F_{\text{dark}2}$), revealed virtually no signal.

Modelling time-dependent conformational changes

Given the time-resolved changes evident in difference electron density maps, we next sought to model the specific structural changes that give rise to those signals. Because the nature of difference density signals differed substantially as a function of pump–probe time delay, we used distinct approaches to model signals appearing on the nanosecond and microsecond timescales.

As noted, the dominant difference density features that we observed at the 20 ns pump–probe time delay manifested as negative peaks over atomic positions, surrounded by positive halos (Fig. 3a, Extended Data Fig. 1a and Supplementary Video 4). We hypothesized that these features corresponded to an overall increase in atomic B-factors resulting from increased thermal motion following T-jump, because the subtraction of a taller but narrower Gaussian function from one that has the same area under the curve but is shorter and broader would produce a difference function with a similar shape. To test this hypothesis, we used two sets of structure factors calculated from our dark state model. Specifically, we calculated one set of structure factors directly from the atomic coordinates and refined B-factors, and a second set of structure factors from the same coordinates, but with B-factors that had been scaled by a factor of 1.2, representing a 20%

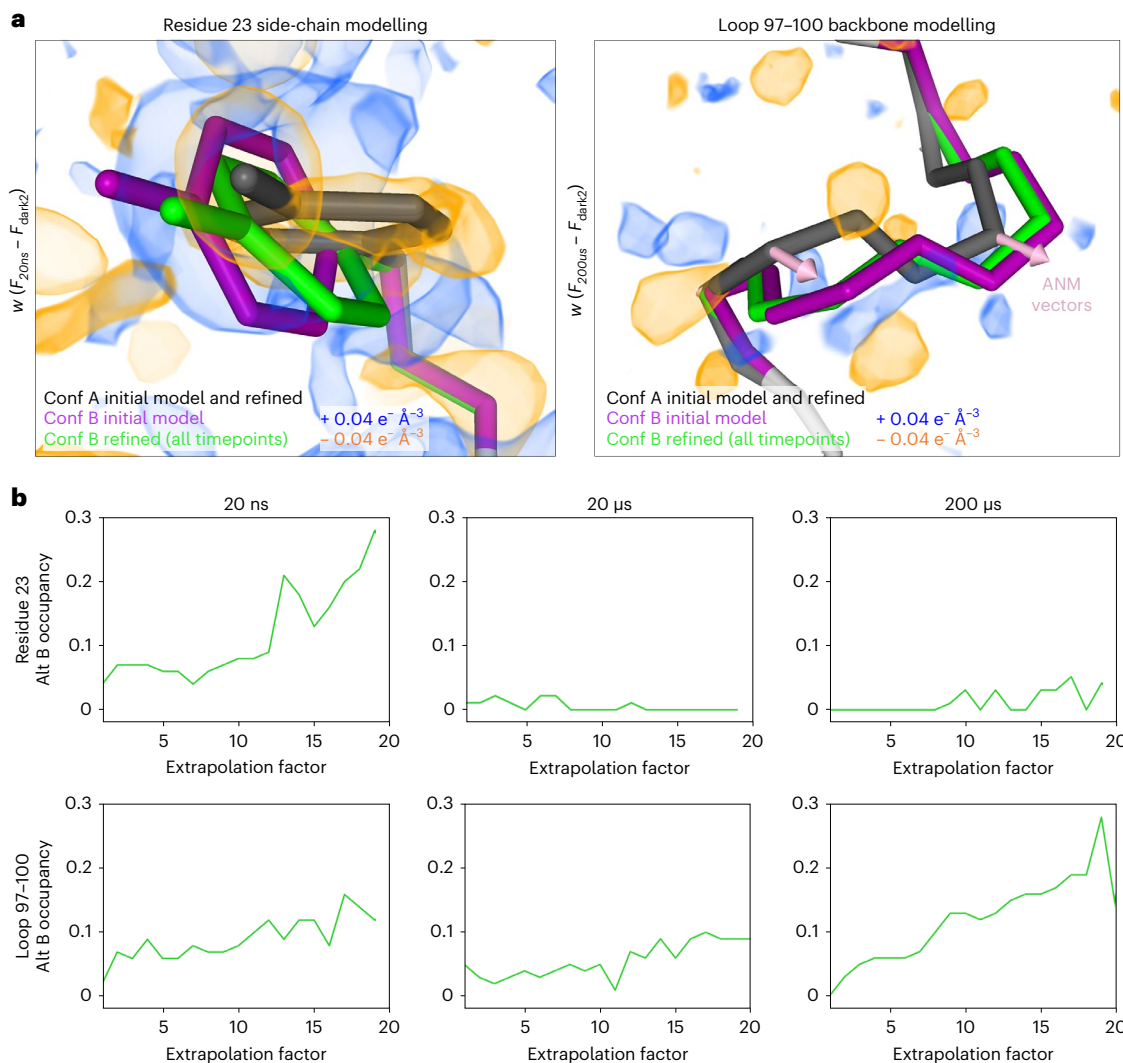


Fig. 4 | Explicit modelling of time-resolved structural changes. **a**, For all pump–probe time delays, difference electron density maps were visualized at an absolute contour level of $\pm 0.04 \text{ e}^{-} \text{ Å}^{-3}$ alongside the refined models. Alternate conformations were manually modelled into the experimental difference density for several regions, including residues 23 and 97–100, then refined against ESFMs. An ANM was developed on the basis of the ground state (conformation

A of the initial model) and vectors were visualized for comparison with alternate conformers. **b**, Occupancies of the alternative conformations were examined as a function of increasing extrapolation factors. The stability of the hypothetical high-energy states during the coordinate refinement, and the increase in their occupancies with increasing extrapolation factor provide evidence that these conformations are populated in the ensemble.

increase. We then used these sets of calculated structure factors to generate a difference map showing how an increase in B-factors due to a T-jump would manifest in the electron density, and noted a striking similarity with the experimentally derived map (Extended Data Fig. 2 and Supplementary Video 5). We determined the RSCC between this hypothetical map and the map calculated from our 20 ns T-jump data and found extremely good agreement (CC 0.67, Extended Data Fig. 1b). Systematic comparison of this simulated difference map to experimentally derived difference maps, via RSCCs, revealed additional similarities (Extended Data Fig. 1b). The simulated map has a weaker, but still significant, correlation with 20 μs and 200 μs experimental difference maps (0.33 and 0.37, respectively), probably corresponding to negative peaks appearing at atom positions as electron density moves away from these locations.

Next, using difference maps as a guide, set at a contour level of $0.04 \text{ e}^{-} \text{ Å}^{-3}$ to match our IADDAT analysis, we manually built alternative conformations for several regions of the protein where the difference density could be interpreted explicitly, including residue 23 (inspired by the 20 ns difference map) and a short loop composed of residues

97–100 that lies at the end of an α-helix adjacent to the active site (inspired by the 200 μs difference map) (Fig. 4a). We included these alternative conformations in a multi-conformer model, and conducted an additional series of refinements against ‘extrapolated’ structure factor magnitudes (ESFMs)^{27,28} to assess whether the alternative conformations could represent high-energy states of the enzyme. The procedure used to generate datasets containing ESFMs is described in equations (1) and (2), and has been implemented by others^{5,6}. Briefly, we multiplied the weighted experimental structure factor difference, $w(F_t - F_{\text{dark}_2})$, for a given pump–probe time delay by an arbitrary extrapolation factor (N), and then added that product to the structure factors measured for the dark state (F_{dark_2}). This manipulation of the experimental data effectively scales up the contribution of high-energy states of the molecule that are populated by T-jump to the overall structure factor magnitudes. For each pump–probe time delay in our T-jump series, we refined our model, containing the dark state structure and potential high-energy conformations, against a series of ESFM sets generated with increasing extrapolation factors (Methods). Following refinement of coordinates, B-factors and occupancies, we observed that the major

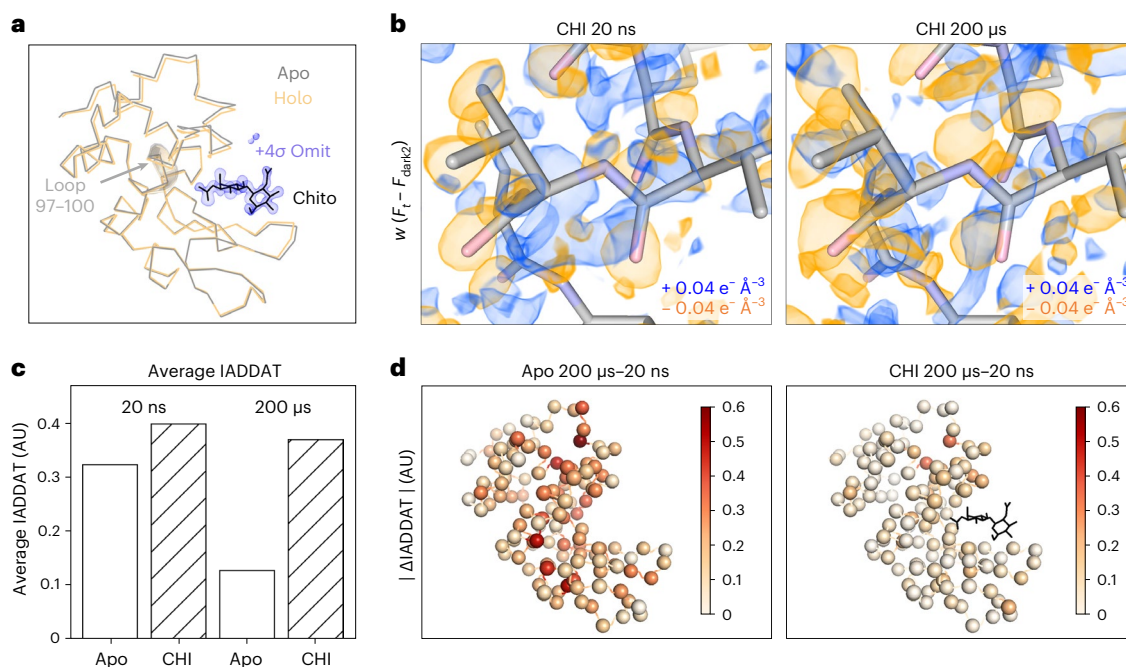


Fig. 5 | Chitobiose binding perturbs changes induced by T-jump. **a**, Ribbon diagrams of lysozyme structures (laser off) in the apo (grey) and chitobiose (CHI)-bound (holo, orange) forms show a decrease in distance between the two lobes of the protein upon ligand binding, characteristic of the active site ‘closing’ motion. Chitobiose is shown as black sticks, along with a ligand omit map contoured to $+4\sigma$ and carved within 5 Å of the chitobiose molecule. **b**, Visualization of weighted difference density maps ($F_t - F_{dark2}$) for chitobiose-bound datasets show similar in the apo and ligand-bound states. Maps were

visualized at an absolute contour level of ± 0.04 e⁻ Å⁻³ alongside initial refined models for each pump–probe time delay. **c**, Comparing average IADDAT values for ligand-bound and apo maps revealed similar signal levels at 20 ns, with substantial differences appearing by 200 μs. **d**, Mapping absolute differences in IADDAT between 20 ns and 200 μs ($|\Delta IADDAT|$) values onto the structure (C-alphas as spheres) further reveals that time-resolved changes are more pronounced for the apo enzyme than for the inhibitor-bound enzyme.

dark state conformation was unperturbed and that the alternative conformations moved very little (Fig. 4a and Supplementary Videos 6 and 7). We investigated the occupancies of these conformations as a function of extrapolation factor (Fig. 4b), and noticed that occupancies of the novel conformers generally increased as a function of extrapolation factor. This observation further confirms the correlation between the modelled molecular motions and laser-induced changes to the structure factors, but also suggested that only a very small fraction of protein molecules have transitioned to higher energy conformational states, because we were not able to extrapolate enough to model the high-energy state at full occupancy. The need to apply large extrapolation factors, combined with the fact that temperature-induced conformational changes are dispersed throughout the unit cell rather than concentrated near a chromophore, limit these refinements against ESFM²⁷. Nevertheless, using this approach, we could detect specific molecular motions, including short amplitude motions (for example, rotation of Tyr23) that were most evident at the 20 ns pump–probe time delay, and larger motions (for example the backbone shift of loop 97–100) that were most evident in the 200 μs dataset. The backbone shift that we detected for residues 97–100 in the 200 μs difference electron density map was consistent with backbone motion calculated by normal mode analysis of the ground state structure (Fig. 4a and Extended Data Fig. 3).

Inhibitor binding alters T-jump-induced dynamics

In addition to the datasets described above, we also examined analogous data for lysozyme bound to a naturally occurring inhibitor, chitobiose, which is known to bind to the active site and stabilize a ‘closed’ form of the enzyme (Fig. 5a). Specifically, for chitobiose-bound crystals, we collected T-jump data corresponding to two pump–probe time delays (20 ns and 200 μs; Extended Data Table 4). Time-resolved

difference maps calculated for chitobiose-bound crystals revealed an altered dynamic response to T-jump relative to the apo crystals (Fig. 5b). Qualitatively, while the 20 ns difference density looks similar for both apo and chitobiose-bound crystals, marked differences are evident by 200 μs. In the case of the apo enzyme, features in the time-resolved difference maps change substantially between 20 ns and 200 μs. In contrast, when chitobiose is bound, the features in the time-resolved difference maps change relatively little between 20 ns and 200 μs (Fig. 5b). These observations were confirmed quantitatively using IADDAT calculations. Specifically, we looked at the overall difference in IADDAT ($|\Delta IADDAT|$) between the 20 ns and 200 μs time delays for both the apo and chitobiose-bound crystals (Fig. 5c,d). We observed that the difference in IADDAT as a function of pump–probe time delay is much more pronounced for the apo enzyme relative to when the inhibitor is bound. RSCL calculations further confirmed these observations, showing high pairwise correlations between the apo 20 ns, chitobiose-bound 20 ns and chitobiose-bound 200 μs difference maps, each of which have a much weaker correlation with the apo 200 μs difference map (Extended Data Fig. 1b).

Discussion

The results presented here demonstrate that infra-red laser-induced T-jump can be used as an effective perturbation method for TRX to map the dynamics of a biological macromolecule at atomic resolution. We performed pump–probe SFX using a nanosecond pulsed laser, tuned to mid-IR wavelengths (1,443 nm), to rapidly heat the solvent surrounding and permeating microcrystals of the dynamic enzyme lysozyme (40.7% solvent), and monitored the resulting molecular motions using ultrafast X-ray pulses from an XFEL. Using algebraic tools, leveraged from previous solution X-ray scattering experiments²³, we detected the introduction of a T-jump, which was corroborated by observations

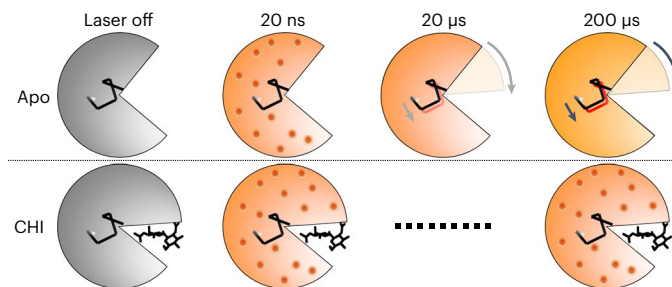


Fig. 6 | Schema of time-resolved conformational changes in lysozyme following T-jump.

The cartoon highlights closure of the active site cleft upon chitobiose (CHI) binding, with subsequent representations of time-resolved structural changes following T-jump. At short pump–probe time delays (20 ns) atomic vibrations (shown as red dots) are present in both the apo and inhibitor-bound structures. These vibrations persist in the inhibitor-bound structure but dissipate into more complex motions in the apo structure, including the bending of a helix that lies at the hinge point of the lysozyme molecule.

contains the least evidence for high-energy conformations in both IADDAT and ESFM refinement analyses. The lack of strong difference density at this pump–probe time delay probably results from a mixture of high-energy conformational states being populated within tens of microseconds, before the ensemble narrows once again as the system approaches a new thermal equilibrium within hundreds of microseconds. This notion is consistent with single-molecule measurements that revealed large amplitude motions in lysozyme occur along multiple distinct trajectories with different transition times and intermediates⁵².

To assess whether our analysis detected functional protein motions, rather than spurious thermal fluctuations, we performed T-jump measurements in the presence of an orthogonal perturbation to the enzyme's functional dynamics; specifically, the binding of chitobiose. Chitobiose is a natural inhibitor of lysozyme that mimics the bound substrate and shifts the enzyme's conformational equilibrium toward the more compact 'closed' state in which the two lobes of the enzyme clamp down on the carbohydrate in the active site^{43,44}. We observed, both visually and quantitatively using real-space map correlations (Extended Data Fig. 2b), that difference electron density maps corresponding to the 20 ns pump–probe time delay look similar for both the apo and chitobiose-bound datasets, demonstrating that the fast onset of short-amplitude motions is similar in both cases. However, at the long time delay (200 μs), the difference electron density maps calculated from the chitobiose-bound data do not show evidence for dissipation of short amplitude motions into larger-scale conformational changes, as seen for the apo enzyme, but instead, remain similar to the maps corresponding to short (20 ns) pump–probe time delays (Extended Data Fig. 1b). Additionally, the B-factors of the chitobiose-bound model remain high when refined against data corresponding to the 200 μs time delay relative to the apo model (Extended Data Fig. 4). The inhibitor is known to restrict larger-amplitude motions (for example, hinge bending) related to substrate binding and catalysis, locking it in a 'closed' conformation. Accordingly, the presence of the inhibitor does not affect the rapid onset of thermal motion through the enzyme, but it does abolish the time-resolved changes that we attribute to microsecond functional motions (Fig. 6), probably pushing them to the millisecond or longer timescale, outside the window of observation for our experiment. Corroborating our model, nuclear magnetic resonance spectroscopy has shown that binding of a similar carbohydrate inhibitor (chitotriose) to lysozyme has little effect on the global ps–ns motions⁴⁷, while FRET experiments reveal that inter-domain dynamics are slowed substantially in the presence of substrate.

The work described here demonstrates that T-jump can be used as an effective perturbation to resolve conformational dynamics at atomic resolution using TRX. While limited in temporal resolution, our results allow the coarse mapping of dynamics in hen egg-white lysozyme across four logarithmic decades of time. While the structure of hen egg-white lysozyme has been studied extensively by X-ray crystallography for many years, most experiments that have measured lysozyme dynamics with kinetic detail have been performed on the analogous T4 lysozyme⁴⁸. Our observations begin to close this gap by revealing dynamics on similar timescales in the two enzymes. Because temperature change is a universal method to perturb molecular motion, we anticipate that T-jump crystallography will be applied to other systems that can undergo functional conformational changes in the crystal lattice, opening the door for broad exploration of macromolecular dynamics. While our initial experiments offer promise for the use of T-jump as a perturbation in TRX, they also highlight some of the key challenges that remain. Specifically, the large time requirement per dataset in a TRX experiment is a current limitation for achieving high temporal resolution. Improvements in the speed of data collection will enable a more detailed exploration of the time domain, as reported for T-jump X-ray solution scattering experiments²³. Additionally, because T-jump induces structural changes that

of unit cell thermal expansion and increased atomic displacements (higher refined B-factors). Next, we implemented a series of analyses common in time-resolved protein crystallography, including calculation of uncertainty-weighted difference electron density maps²⁶, spatial integration of difference electron density^{5,42}, and refinement against ESFMs^{27,28}, allowing us to identify high-energy conformational states of the protein, and to estimate the timescales on which they are populated.

The goal of a T-jump crystallography experiment is to map the structural dynamics of the crystallized molecule. We selected lysozyme as our subject for this initial study, because it crystallizes easily, diffracts well, and is known to undergo a characteristic hinge-bending motion that results in domain closure around the active site^{43,44}. Although limited in temporal resolution, the data we collected and the analyses we performed provide a coarse-grained model for the evolution of conformational dynamics in lysozyme following T-jump that is consistent with published literature on lysozyme dynamics^{43,45}. Our analysis of experimental maps supports a rapid increase in atomic displacement parameters (B-factors) within 20 ns of the pump laser pulse, evidence of increased harmonic motion resulting from heat transfer to the protein from the thermally excited solvent. The spatial distribution of difference electron density features at very short pump–probe time delays (for example, 20 ns) is not uniform (Figs. 3a,b and 5b,d) suggesting that heat flows more readily into some regions of the lysozyme molecule than others. We also modelled high-energy conformations directly from time-resolved difference electron density maps and refined them against ESFMs. This analysis revealed motions such as rotamer flips on fast timescales (for example, 20 ns), and larger motions, including correlated shifts of loops spanning multiple residues, on slower timescales (for example, 200 μs). The most noticeable of these movements includes a short loop encompassing residues 97–100, which is at the end of an α-helix adjacent to the active site and known to be mobile during lysozyme hinge bending⁴⁶ (Fig. 5a). These observations yield a model wherein T-jump first excites harmonic thermal motions and short-amplitude anharmonic motions, such as rotamer flips, on the nanosecond timescale. In a small population of molecules, these fast motions are subsequently converted to larger-scale conformational changes that are linked to the catalytic cycle, such as loop displacements (for example, residues 97–100) that occur on the microsecond (or longer) timescale and are coupled to the active site (Fig. 6)⁴⁷. Our observations are in agreement with a variety of other kinetic measurements performed on the architecturally similar, but evolutionarily unrelated, T4 lysozyme⁴⁸, including single-molecule techniques, that demonstrated protein motions with transition times in the range of tens to hundreds of microseconds^{49–51}. Notably, the intermediate pump–probe time delay (20 μs) in our limited time series

can be distributed across the entire unit cell, rather than concentrated at a specific site (for example, a chromophore or ligand-binding site), refinement methods that utilize ESFMs do not perform well because there is a significant phase difference between structure factors for the dark state and for the high-energy states that are populated during T-jump²⁷. Simultaneous refinement of extrapolated structure factor magnitudes and phases will improve our ability to accurately model high-energy conformations from TRX data. With future technological developments forthcoming, and T-jump available as a general perturbation method, TRX experiments will become more relevant to a wider audience of structural biologists.

Online content

Any methods, additional references, Nature Portfolio reporting summaries, source data, extended data, supplementary information, acknowledgements, peer review information; details of author contributions and competing interests; and statements of data and code availability are available at <https://doi.org/10.1038/s41557-023-01329-4>.

References

1. Henzler-Wildman, K. & Kern, D. Dynamic personalities of proteins. *Nature* **450**, 964–972 (2007).
2. Bhabha, G., Biel, J. T. & Fraser, J. S. Keep on moving: discovering and perturbing the conformational dynamics of enzymes. *Acc. Chem. Res.* **48**, 423–430 (2015).
3. van den Bedem, H. & Fraser, J. S. Integrative, dynamic structural biology at atomic resolution—it's about time. *Nat. Methods* **12**, 307–318 (2015).
4. Coquelle, N. et al. Chromophore twisting in the excited state of a photoswitchable fluorescent protein captured by time-resolved serial femtosecond crystallography. *Nature Chem.* **10**, 31–37 (2018).
5. Hekstra, D. R. et al. Electric-field-stimulated protein mechanics. *Nature* **540**, 400–405 (2016).
6. Genick, U. K. et al. Structure of a protein photocycle intermediate by millisecond time-resolved crystallography. *Science* **275**, 1471–1475 (1997).
7. Schlichting, I. et al. Time-resolved X-ray crystallographic study of the conformational change in Ha-Ras p21 protein on GTP hydrolysis. *Nature* **345**, 309–315 (1990).
8. Srager, V. et al. Photolysis of the carbon monoxide complex of myoglobin: nanosecond time-resolved crystallography. *Science* **274**, 1726–1729 (1996).
9. Schmidt, M. Time-resolved macromolecular crystallography at modern X-ray sources. *Methods Mol. Biol.* **1607**, 273–294 (2017).
10. Neutze, R. & Moffat, K. Time-resolved structural studies at synchrotrons and X-ray free electron lasers: opportunities and challenges. *Curr. Opin. Struct. Biol.* **22**, 651–659 (2012).
11. Orville, A. M. Recent results in time resolved serial femtosecond crystallography at XFELs. *Curr. Opin. Struct. Biol.* **65**, 193–208 (2020).
12. Josts, I. et al. Photocage-initiated time-resolved solution X-ray scattering investigation of protein dimerization. *IUCrJ* **5**, 667–672 (2018).
13. Olmos, J. L. et al. Enzyme intermediates captured ‘on the fly’ by mix-and-inject serial crystallography. *BMC Biol.* **16**, 59 (2018).
14. Fenimore, P. W., Frauenfelder, H., McMahon, B. H. & Parak, F. G. Slaving: solvent fluctuations dominate protein dynamics and functions. *Proc. Natl Acad. Sci. USA* **99**, 16047–16051 (2002).
15. Keedy, D. A. et al. Mapping the conformational landscape of a dynamic enzyme by multitemperature and XFEL crystallography. *eLife Sci.* **4**, e07574 (2015).
16. Keedy, D. A. et al. An expanded allosteric network in PTP1B by multitemperature crystallography, fragment screening, and covalent tethering. *eLife* **7**, e36307 (2018).
17. Wang, J. & El-Sayed, M. A. Temperature jump-induced secondary structural change of the membrane protein bacteriorhodopsin in the premelting temperature region: a nanosecond time-resolved Fourier transform infrared study. *Biophys. J.* **76**, 2777–2783 (1999).
18. Meadows, C. W., Balakrishnan, G., Kier, B. L., Spiro, T. G. & Klinman, J. P. Temperature-jump fluorescence provides evidence for fully reversible microsecond dynamics in a thermophilic alcohol dehydrogenase. *J. Am. Chem. Soc.* **137**, 10060–10063 (2015).
19. Gillespie, B. et al. NMR and temperature-jump measurements of de novo designed proteins demonstrate rapid folding in the absence of explicit selection for kinetics. *J. Mol. Biol.* **330**, 813–819 (2003).
20. Ma, H., Wan, C. & Zewail, A. H. Ultrafast T-jump in water: studies of conformation and reaction dynamics at the thermal limit. *J. Am. Chem. Soc.* **128**, 6338–6340 (2006).
21. Rubtsov, I. V. & Burin, A. L. Ballistic and diffusive vibrational energy transport in molecules. *J. Chem. Phys.* **150**, 020901 (2019).
22. Butterfoss, G. L. & Hermans, J. Boltzmann-type distribution of side-chain conformation in proteins. *Protein Sci. A* **12**, 2719 (2003).
23. Thompson, M. C. et al. Temperature-jump solution X-ray scattering reveals distinct motions in a dynamic enzyme. *Nat. Chem.* **11**, 1058–1066 (2019).
24. Cho, H. S. et al. Dynamics of quaternary structure transitions in R-state carbonmonoxyhemoglobin unveiled in time-resolved X-ray scattering patterns following a temperature jump. *J. Phys. Chem. B* **122**, 11488–11496 (2018).
25. Hori, T. et al. The initial step of the thermal unfolding of 3-isopropylmalate dehydrogenase detected by the temperature-jump Laue method. *Protein Eng.* **13**, 527–533 (2000).
26. Ursby, T. & Bourgeois, D. Improved estimation of structure-factor difference amplitudes from poorly accurate data. *Acta Crystallogr. A* **53**, 564–575 (1997).
27. Genick, U. K. Structure-factor extrapolation using the scalar approximation: theory, applications and limitations. *Acta Crystallogr. D* **63**, 1029–1041 (2007).
28. De Zitter, E., Coquelle, N., Oeser, P., Barends, T. R. M. & Colletier, J.-P. Xtrapol8 enables automatic elucidation of low-occupancy intermediate-states in crystallographic studies. *Commun. Biol.* **5**, 1–11 (2022).
29. Boutet, S. et al. High-resolution protein structure determination by serial femtosecond crystallography. *Science* **337**, 362–364 (2012).
30. Kubo, M. et al. Nanosecond pump–probe device for time-resolved serial femtosecond crystallography developed at SACLAC. *J. Synchrotron. Rad.* **24**, 1086–1091 (2017).
31. Nango, E., Kubo, M., Tono, K. & Iwata, S. Pump–probe time-resolved serial femtosecond crystallography at SACLAC: current status and data collection strategies. *Appl. Sci.* **9**, 5505 (2019).
32. Beitz, J. V., Flynn, G. W., Turner, D. H. & Sutin, N. Stimulated Raman effect. A new source of laser temperature-jump Heating. *J. Am. Chem. Soc.* **92**, 4130–4132 (1970).
33. Sugahara, M. et al. Hydroxyethyl cellulose matrix applied to serial crystallography. *Sci. Rep.* **7**, 703 (2017).
34. Shimazu, Y. et al. High-viscosity sample-injection device for serial femtosecond crystallography at atmospheric pressure. *J. Appl. Cryst.* **52**, 1280–1288 (2019).
35. Ishikawa, T. et al. A compact X-ray free-electron laser emitting in the sub-ångström region. *Nat. Photonics* **6**, 540–544 (2012).
36. Kameshima, T. et al. Development of an X-ray pixel detector with multi-port charge-coupled device for X-ray free-electron laser experiments. *Rev. Sci. Instrum.* **85**, 033110 (2014).

37. Nakane, T. et al. Data processing pipeline for serial femtosecond crystallography at SACLA. *J Appl Cryst.* **49**, 1035–1041 (2016).
38. Grosse-Kunstleve, R. W., Sauter, N. K., Moriarty, N. W. & Adams, P. D. The Computational Crystallography Toolbox: crystallographic algorithms in a reusable software framework. *J. Appl. Cryst.* **35**, 126–136 (2002).
39. Winter, G. et al. DIALS: implementation and evaluation of a new integration package. *Acta Crystallogr. D* **74**, 85–97 (2018).
40. Brewster, A. S. et al. Improving signal strength in serial crystallography with DIALS geometry refinement. *Acta Crystallogr. D* **74**, 877–894 (2018).
41. Sauter, N. K. XFEL diffraction: developing processing methods to optimize data quality. *J. Synchrotron. Rad.* **22**, 239–248 (2015).
42. Wickstrand, C. et al. A tool for visualizing protein motions in time-resolved crystallography. *Struct. Dyn.* **7**, 024701 (2020).
43. Mccammon, J. A., Gelin, B. R., Karplus, M. & Wolynes, P. G. The hinge-bending mode in lysozyme. *Nature* **262**, 325–326 (1976).
44. Mchaourab, H. S., Oh, K. J., Fang, C. J. & Hubbell, W. L. Conformation of T4 lysozyme in solution. Hinge-bending motion and the substrate-induced conformational transition studied by site-directed spin labeling. *Biochemistry* **36**, 307–316 (1997).
45. De Simone, A., Montalvo, R. W., Dobson, C. M. & Vendruscolo, M. Characterization of the interdomain motions in hen lysozyme using residual dipolar couplings as replica-averaged structural restraints in molecular dynamics simulations. *Biochemistry* **52**, 6480–6486 (2013).
46. Brooks, B. & Karplus, M. Normal modes for specific motions of macromolecules: application to the hinge-bending mode of lysozyme. *Proc. Natl Acad. Sci. USA* **82**, 4995–4999 (1985).
47. Moorman, V. R., Valentine, K. G. & Wand, A. J. The dynamical response of hen egg white lysozyme to the binding of a carbohydrate ligand. *Protein Sci.* **21**, 1066–1073 (2012).
48. Matthews, B. W., Remington, S. J., Grüter, M. G. & Anderson, W. F. Relation between hen egg white lysozyme and bacteriophage T4 lysozyme: evolutionary implications. *J. Mol. Biol.* **147**, 545–558 (1981).
49. Yirdaw, R. B. & McHaourab, H. S. Direct observation of T4 lysozyme hinge-bending motion by fluorescence correlation spectroscopy. *Biophys. J.* **103**, 1525–1536 (2012).
50. Akhterov, M. V. et al. Observing lysozyme's closing and opening motions by high-resolution single-molecule enzymology. *ACS Chem. Biol.* **10**, 1495–1501 (2015).
51. Sanabria, H. et al. Resolving dynamics and function of transient states in single enzyme molecules. *Nat. Commun.* **11**, 1231 (2020).
52. Lu, M. & Lu, H. P. Revealing multiple pathways in T4 lysozyme substep conformational motions by single-molecule enzymology and modeling. *J. Phys. Chem. B* **121**, 5017–5024 (2017).

Publisher's note Springer Nature remains neutral with regard to jurisdictional claims in published maps and institutional affiliations.

Open Access This article is licensed under a Creative Commons Attribution 4.0 International License, which permits use, sharing, adaptation, distribution and reproduction in any medium or format, as long as you give appropriate credit to the original author(s) and the source, provide a link to the Creative Commons license, and indicate if changes were made. The images or other third party material in this article are included in the article's Creative Commons license, unless indicated otherwise in a credit line to the material. If material is not included in the article's Creative Commons license and your intended use is not permitted by statutory regulation or exceeds the permitted use, you will need to obtain permission directly from the copyright holder. To view a copy of this license, visit <http://creativecommons.org/licenses/by/4.0/>.

© The Author(s) 2023

¹Department of Chemistry and Biochemistry, University of California, Merced, Merced, CA, USA. ²RIKEN SPring-8 Center, Sayo-gun, Japan. ³Institute of Multidisciplinary Research for Advanced Materials, Tohoku University, Aoba-ku, Japan. ⁴Department of Bioengineering and Therapeutic Sciences, University of California, San Francisco, San Francisco, CA, USA. ⁵Molecular Biophysics and Integrated Bioimaging Division, Lawrence Berkeley National Laboratory, Berkeley, CA, USA. ⁶Department of Life Science, Graduate School of Science, University of Hyogo, Hyogo, Japan. ⁷Laboratory for Drug Discovery, Pharmaceuticals Research Center, Asahi Kasei Pharma Corporation, Izunokuni-shi, Japan. ⁸SLAC National Accelerator Laboratory, Linac Coherent Light Source, Menlo Park, CA, USA. ⁹Department of Electrical and Computer Engineering, University of California, Los Angeles, Los Angeles, CA, USA. ¹⁰Department of Chemistry and Biotechnology, Graduate School of Engineering, Tottori University, Tottori, Japan. ¹¹Center for Research on Green Sustainable Chemistry, Tottori University, Tottori, Japan. ¹²Department of Biochemistry and Biophysics, University of California San Francisco, San Francisco, CA, USA. ¹³Stanford Synchrotron Radiation Lightsource, SLAC National Accelerator Laboratory, Menlo Park, CA, USA. ¹⁴Department of Cell Biology, Graduate School of Medicine, Kyoto University, Yoshidakonoe-cho, Sakyo-ku, Japan. ¹⁵Structural Biology Research Center, Institute of Materials Structure Science, KEK/High Energy Accelerator Research Organization, Tsukuba, Japan. ¹⁶Japan Synchrotron Radiation Research Institute, Hyogo, Japan. ¹⁷Present address: Department of Integrative Structural and Computational Biology, Scripps Research, San Diego, CA, USA. ¹⁸Present address: Ginward Japan K.K., Tokyo, Japan. ✉ e-mail: eriko.nango.c4@tohoku.ac.jp; mthompson30@ucmerced.edu

Methods

Lysozyme crystallization

Lysozyme was crystallized in batch by mixing a 20 mg ml⁻¹ solution (lyophilized enzyme dissolved in 0.1 M sodium acetate at pH 3.0) with precipitant (28% (w/v) NaCl, 8% (w/v) PEG6000 and 0.1 M sodium acetate at pH 3.0) in a 1:1 ratio⁵³. For inhibitor-bound structures *N,N'*-diacetylchitobiose was included at 10 mg ml⁻¹ with the Lysozyme solution before mixture with precipitant. Both apo and chitobiose-bound crystals were approximately 10 µm. Before storage, slurries were centrifuged at 4 °C and 3,000g for 3 min, the supernatant was removed and crystals were resuspended in 10% (w/v) NaCl and 1.0 M sodium acetate (pH 3.0).

Sample delivery and data collection

We collected data at SACLA³⁵ using the Diverse Application Platform for Hard X-ray Diffraction in SACLA (DAPHNIS)⁵⁴ at BL2 (ref. 55). Before data collection, crystal slurries were centrifuged, the supernatant was removed, and crystals were directly mixed (in a 1:9 ratio) with a viscogen-containing crystal stabilization buffer with an additional 18% hydroxyethyl cellulose³³. The mixture was then loaded into the reservoir of a sample injector device³⁴. This device amplifies pressure generated by an HPLC pump to extrude the viscous medium carrying crystals through a microfluidic nozzle with a diameter of 75 µm. The linear flow rate of this stream was 9.43 mm s⁻¹, with a volumetric flow rate of 2.5 µl min⁻¹. Helium gas was streamed as a sheath for the liquid jet, with He flow adjusted as needed to maintain a stable stream of lysozyme microcrystals.

X-ray diffraction measurements were made using 0.6 mJ XFEL pulses 10 fs in duration, with a peak photon energy of 9.5 keV. Diffraction images were collected at 30 Hz using a custom-built 4 M pixel detector with multi-port CCD (mpCCD) sensors³⁶. For time-resolved datasets, crystals were rapidly heated by excitation of the water O–H stretch with mid-IR laser light (1,443 nm, 7 ns pulse duration, 540 µJ pulse energy, ~50 µm (full width at half maximum) focus diameter (Supplementary Fig. 1), at defined time delays before X-ray exposure. Although the absorption peak at ~1,443 nm is not the strongest mid-IR absorption peak for liquid water, it was selected as a compromise between large T-jumps and uniform heating of the sample, because greater absorption leads to greater increase of thermal energy but also leads to more dramatic temperature gradients through the sample. The IR pump laser operated at a repetition rate of 10 Hz, so data were collected with two dark diffraction measurements interleaved between each T-jump measurement^{30,31}. An IR camera was used to monitor the alignment of the pump laser with the sample, and the firing of the laser was verified by reflecting a small amount of the laser light to a photodiode. Both the jet stream and the pump laser beam were centred on the position of the X-ray beam, which was focused to a diameter of 1.5 µm, much smaller than both the jet and the pump laser. The direction of the IR laser beam was approximately 45° off-axis from the XFEL beam. Data collection parameters were consistent across timepoints and samples (apo versus chitobiose-bound).

Processing of bragg reflections

Data collection was supported by a real-time data processing pipeline³⁷ developed on Cheetah⁵⁶ and CrystFEL⁵⁷. Images identified as hits were processed using methods from CCTBX³⁸. For Bragg processing, data were indexed and integrated using dials.stills_process³⁹. Initial indexing results were used to refine the detector model, as well as crystal models⁴⁰. Refinement of the detector distance and panel geometry improved the agreement between measured and predicted spots. Bragg data were then merged and post-refined using cxi.merge⁴¹. Error estimates were treated according to the Ev11 method^{40,58}, wherein error estimates were increased using terms refined from the measurements until they could better explain the uncertainty observed in the merged reflection intensities. A total of 17 merged datasets were produced

from our experiment. For the apo enzyme, we collected one ‘laser off’ dataset, and explored three pump–probe time delays (20 ns, 20 µs and 200 µs), including a ‘laser on’ dataset and two interleaved control datasets (dark1 and dark2) for each time delay. For the chitobiose-bound enzyme, we collected one ‘laser off’ dataset, and explored two pump–probe time delays (20 ns and 200 µs), with corresponding interleaved control datasets (dark1 and dark2).

Processing and analysis of solvent scattering

For analysis of solvent scattering, each image identified as a hit by Cheetah was processed into an azimuthal average using dxtbx.radial_average. The function was modified to include a sliding one-dimensional median filter, with a window size of 15 *q* bins. The median filter minimized contributions of the Bragg peaks to the radial average while preserving the solvent scattering signal. Individual scattering curves were culled from later SVD analysis based on collection anomalies (clogging of sample jet and so on), since these contributions dominated variations in the background signal, making detection of T-jumps difficult. A series of custom scripts were written to process and analyse the solvent scattering curves³⁹. Briefly, one-dimensional X-ray scattering curves were pooled and scaled using an algebraic (least-squares) procedure²³. A mask was applied so that only data between 2.0 Å⁻¹ and 2.5 Å⁻¹ were used for scaling. Scaled curves, containing data between 1.0 Å⁻¹ and 2.7 Å⁻¹, were combined in a 2D matrix, where each row of the matrix represents a unique scattering curve, each column represents a value of *q*, and the entries represent the corresponding azimuthally averaged scattering intensities. This matrix was analysed using SVD^{24,60–62}, where the right singular vectors (*v_n*) represented basis vectors of the observed scattering curves and the left singular vectors (*u_n*) described the contribution of each basis vector to each individual scattering curve. By analysing the values of *u_{ln}*, the entries in *U* that quantify the contribution of the temperature-dependent singular vector (*v_l*) to each scattering curve (*n*), we determined that *u_{ln}* correlated with IR laser status.

Estimation of T-jump

The following calculations assume pure water, which is only an approximation; however, these calculations roughly reproduce the T-jumps that were experimentally measured in prior work²³. Additionally, we note that the heat capacity of crystalline lysozyme is nearly the same as for pure water⁶³, an approximation that neglects the effect of hydroxyethyl cellulose upon IR absorbance.

1. $A_{1443} = 12.83$ for water based on ref. 32; this corresponds to an attenuation depth of ~780 µm.
2. per Beer's law $\epsilon = \frac{A_{1443}}{I \times M} = \frac{12.83}{1.000 \text{ cm} \times 55.56 \text{ M}} = 0.2309 \text{ cm}^{-1} \text{ M}^{-1}$
3. $A_{75\mu\text{m}} = 0.2309 \text{ cm}^{-1} \text{ M}^{-1} (7.5 \times 10^{-3} \text{ cm})(55.56 \text{ M}) = 0.096$
4. $q = I \times A_{75\mu\text{m}} = 5.4 \times 10^{-4} \text{ J} \times 0.096 = 5.2 \times 10^{-5} \text{ J}$
5. Volume = $r^2 \times \pi \times l = 5.0 \times 10^{-3} \text{ cm} \times 5.0 \times 10^{-3} \text{ cm} \times \pi \times 7.5 \times 10^{-3} \text{ cm} = 5.9 \times 10^{-7} \text{ cm}^3 = 5.9 \times 10^{-7} \text{ ml}$
6. $m = 5.9 \times 10^{-7} \text{ ml} \times 1.0 \text{ g ml}^{-1} = 5.9 \times 10^{-7} \text{ g}$
7. $\Delta T = \frac{q}{m \times c} = \frac{5.2 \times 10^{-5} \text{ J}}{5.9 \times 10^{-7} \text{ g} \times 4.184 \text{ J g}^{-1} \text{ K}^{-1}} = 21 \text{ K}$

We note that the calculated value of 21 K probably represents the maximum T-jump achieved.

Initial model building

All data as output from cxi.merge were converted from intensities to structure factors using phenix.reflection_file_converter. Initial phases for each of the 17 datasets (see above) were calculated via molecular replacement using Phaser⁶⁴, with PDB entry 1IEE as the search model. R-free flags were carried over from PDB entry 1IEE, and random atomic displacements (0.5 Å) were applied to the coordinates to remove model bias before an initial round of refinement. Iterative model building

using Coot followed by refinement in PHENIX⁶⁵ was conducted until the structures converged⁶⁶. The structures refined against the raw F_{dark} and F_t structure factors were deposited to the PDB). Data collection and refinement statistics for these structures are provided in Extended Data Tables 2–5.

Calculation of weighted difference electron density maps

Data were collected in an interleaved fashion (light, dark1 and dark2) as described above, thus for each pump–probe time delay we calculated an ($F_t - F_{\text{dark}2}$) and control ($F_{\text{dark}1} - F_{\text{dark}2}$) difference structure factors. Difference structure factors were weighted^{5,27,67} using Reciprocalspaceship⁶⁸.

$$w_{hkl} = \left[1 + \frac{\sigma^2(\Delta F)}{\langle \sigma^2(\Delta F) \rangle} + 0.05 \frac{|\Delta F|^2}{\langle |\Delta F|^2 \rangle} \right]^{-1} \quad (1)$$

Map phases were calculated using models refined against F_t .

Calculation of IADDAT

Finalized difference electron density maps were integrated for the experimental and control datasets for each pump–probe time delay. Briefly, maps were calculated on a common grid using Reciprocalspaceship⁶⁸, with the unit cell sampled using a grid resolution factor corresponding to $0.25 \times d_{\min}$. Map voxels containing $|\rho| \geq 0.04 \text{ e}^{-\text{\AA}^{-3}}$ and within 2.5 \AA of the atomic model were summed and an average value was calculated per residue. These values were mapped back onto the corresponding structure or plotted directly as a function of residue number for visualization.

Simulated difference density calculations

To understand how uniform amplification of B-factors might affect difference maps, we simulated data on the basis of the refined laser off structure. The atomic displacement parameters (ADPs) present in the model were scaled up linearly 20% using phenix.pdbtools and stored in a second model file. Structure factors were then calculated for both models using phenix.fmodel, and difference maps ($F_{1.2B} - F_B$) were created using the custom scripts described above.

Difference electron density map correlations

Finalized difference structure factors were created using custom scripts as described above. Structure factors were converted to difference maps using Reciprocalspaceship⁶⁸, maps were sampled on a uniform grid corresponding to $0.25 \times d_{\min}$ for the first map. Maps were then thresholded at $|\rho| \geq 0.04 \text{ e}^{-\text{\AA}^{-3}}$, but map voxels were not ‘flattened’ as a function of distance from the model. Custom Python scripts using Numpy were used to calculate and visualize pairwise correlation coefficients for light and control datasets.

Refinement against ESFMs

ESFMs were calculated using Reciprocalspaceship⁶⁸ by adding the weighted structure factor differences (see equation (1) for the definition of w) back to the dark state structure factors^{5,6}.

$$|F_{\text{ESF}}| = N \times w (|F_t| - |F_{\text{dark}2}|) + |F_{\text{dark}2}| \quad (2)$$

R-free flags were carried over from 1IEE as for the original reflection files. Initial models were prepared for each pump–probe time delay by rigid-body refinement of the laser off structure against ESFMs calculated with $N = 1$. N is the reciprocal of the fraction of molecules occupying the excited conformation^{27,28}. Thus, $N = 1$ is not yet extrapolated but represents the experimental T-jumped state with noise down-weighted (equation (2) and Fig. 1) on a per-structure factor basis (equation (1)).

$$N = \frac{1}{\text{fraction of molecules in excited conformation}} \quad (3)$$

With these initial models of the experimental T-jumped state in hand, alternative conformations representing high-energy states that could be manually interpreted from the difference electron density (for example for residues 23 and 97–100, described in Main) were added to the refined structures. Alternative conformations were labelled as ‘B’ and set to 10% occupancy, while the original refined conformation was set as ‘A’ at 90% occupancy. The resulting multi-conformer structures were then subjected to refinement of coordinates, B-factors and occupancies against ESFMs calculated with extrapolation factors (N) ranging from 1 to 20. Occupancies of relevant conformations were analysed as a function of extrapolation factor ($N = 1, 2, \dots, 19, 20$) using custom Python scripts built upon the GEMMI library⁶⁹. The resulting R-factors from refinement against ESFMs are relatively poor (Supplementary Fig. 2), resulting from inadequacies with the scalar approximation implemented in this procedure^{5,27}; however the stability of the high-energy conformations during the refinements support their accuracy. Due to the generally poor R-factors for these multi-conformer models, we have not deposited them to the PDB; however, they are available on our GitHub page and archived on Zenodo (see below).

Normal mode analysis—ANM development

An anisotropic network model (ANM) was developed using a combination of ProDy⁷⁰ and custom Python scripts. Briefly, the model for the 200 μs timepoint was stripped to conformation A (corresponding to the laser off state). The PDB was then imported into ProDy, where alpha carbons were selected for residues 1–129. An ANM model was calculated using standard settings (cut-off 15.0 and gamma 1.0). The full ANM model (standard setting of top 20 modes) was then combined into a single mode, where each individual mode was scaled by the associated eigenvalue (λ)

$$V_{\text{total}} = \sum_{i=0}^n \sqrt{\frac{1}{\lambda_i}} \times V_i \quad (4)$$

The initial PDB coordinates were then projected along the combined ANM vector and written out to a new PDB file. Finally, the initial and projected coordinates were visualized using PyMOL, with the ANM vectors rendered as arrows between alpha carbons using the custom module, Modevectors⁷¹.

Reporting summary

Further information on research design is available in the Nature Portfolio Reporting Summary linked to this article.

Data availability

Crystallographic models (refined against the raw structure factors as described above) and the associated reflection data have been deposited in the PDB under the following accession codes: 8CVU, 8CVV, 8CVW, 8CW0, 8CW1, 8CW3, 8CW5, 8CW6, 8CW7, 8CW8, 8CWB, 8CWC, 8CWD, 8CWE, 8CWF, 8CWG and 8CWH. The model used for MR is available under accession code 1IEE. Additionally, the raw data are publicly available at CXIDB under ID205. Source data are provided with this paper.

Code availability

All code sufficient to reproduce the analyses described herein, as well as difference density maps and models refined against ESFMs, are available in a GitHub repository (https://github.com/mthompson-lab/Temperature-Jump-Crystallography_Analysis-for-Paper) and archived on Zenodo (<https://doi.org/10.5281/zenodo.7860140>). Code associated with this work was implemented using Python 3 (v3.8.15), and the following libraries were used: numpy v1.19.2, scipy v1.5.2, pandas v1.1.5, matplotlib v3.3.2, seaborn v0.11.1, gemmi v0.4.5, prody v2.3.1 and reciprocalspaceship v0.9.5. Source data are provided with this paper.

References

53. Sugahara, M. et al. Grease matrix as a versatile carrier of proteins for serial crystallography. *Nat. Methods* **12**, 61–63 (2015).
54. Tono, K. et al. Diverse application platform for hard X-ray diffraction in SACLÀ (DAPHNIS): application to serial protein crystallography using an X-ray free-electron laser. *J. Synchrotron Radiat.* **22**, 532–537 (2015).
55. Tono, K., Hara, T., Yabashi, M. & Tanaka, H. Multiple-beamline operation of SACLÀ. *J. Synchrotron Radiat.* **26**, 595–602 (2019).
56. White, T. A. et al. CrystFEL: a software suite for snapshot serial crystallography. *J. Appl. Cryst.* **45**, 335–341 (2012).
57. Barty, A. et al. Cheetah: software for high-throughput reduction and analysis of serial femtosecond X-ray diffraction data. *J. Appl. Cryst.* **47**, 1118–1131 (2014).
58. Evans, P. R. An introduction to data reduction: space-group determination, scaling and intensity statistics. *Acta Crystallogr. D* **67**, 282–292 (2011).
59. xray_thermometer. GitHub https://github.com/fraser-lab/xray_thermometer (2019).
60. Rimmerman, D. et al. Direct observation of insulin association dynamics with time-resolved X-ray scattering. *J. Phys. Chem. Lett.* **8**, 4413–4418 (2017).
61. Kjær, K. S. et al. Introducing a standard method for experimental determination of the solvent response in laser pump, X-ray probe time-resolved wide-angle X-ray scattering experiments on systems in solution. *Phys. Chem. Chem. Phys.* **15**, 15003–15016 (2013).
62. Cammarata, M. et al. Impulsive solvent heating probed by picosecond x-ray diffraction. *J. Chem. Phys.* **124**, 124504 (2006).
63. Miyazaki, Y., Matsuo, T. & Suga, H. Low-temperature heat capacity and glassy behavior of lysozyme crystal. *J. Phys. Chem. B* **104**, 8044–8052 (2000).
64. McCoy, A. J. et al. Phaser crystallographic software. *J. Appl. Cryst.* **40**, 658–674 (2007).
65. Afonine, P. V. et al. Towards automated crystallographic structure refinement with phenix.refine. *Acta Crystallogr. D* **68**, 352–367 (2012).
66. Wolff, A. M. et al. Comparing serial X-ray crystallography and microcrystal electron diffraction (MicroED) as methods for routine structure determination from small macromolecular crystals. *IUCrJ* **7**, 306–323 (2020).
67. Srajer, V. et al. Protein conformational relaxation and ligand migration in myoglobin: a nanosecond to millisecond molecular movie from time-resolved Laue X-ray diffraction. *Biochemistry* **40**, 13802–13815 (2001).
68. Greisman, J. B., Dalton, K. M. & Hekstra, D. R. Reciprocalspaceship: a Python library for crystallographic data analysis. *J. Appl. Cryst.* **54**, 1521–1529 (2021).
69. gemmi. GitHub <https://github.com/project-gemmi/gemmi> (2023).
70. Bakan, A., Meireles, L. M. & Bahar, I. ProDy: protein dynamics inferred from theory and experiments. *Bioinformatics* **27**, 1575–1577 (2011).
71. Modevectors. PyMOLWiki <https://pymolwiki.org/index.php/Modevectors> (2012).

Acknowledgements

We thank T. Nakane for assistance with real-time data analysis, S. Boutet for advice on experimental design and P. Anfinrud for helpful discussions about T-jump experiments. We acknowledge members of the Engineering Team of RIKEN SPring-8 Center for technical support. This work was supported by: grants to M.C.T. and J.S.F. from the NSF BioXFEL Science and Technology Center (STC-1231306); MEXT/JSPS KAKENHI Grants 19H05781 to E.N., 19H05784 to M.K., and 19H05776 to S.I.; the Platform Project for Supporting Drug Discovery and Life Science Research (Basis for Supporting Innovative Drug Discovery and Life Science Research) from Japan Agency for Medical Research and Development under Grant JP21am0101070 to S.I.; and the National Institutes of Health, grant GM117126 to N.K.S. The XFEL experiments were performed at BL2 of SACLÀ with the approval of the Japan Synchrotron Radiation Research Institute (JASRI) (proposal nos. 2017B8055 and 2018A8023).

Author contributions

M.C.T. and J.S.F. conceptualized the experiments. E.N., M.K., K.T., S.I., J.M.H. and N.K.S. contributed resources and methodology. A.M.W., E.N., I.D.Y., M.K., T.N., M.S., S.O., K.I., S.C., T.H., D.I., T.T., R.T., R.G.S., F.Y. and M.C.T. conducted investigations. A.M.W., I.D.Y., A.S.B., B.A.B., A.B., L.J.O., N.K.S. and M.C.T. performed formal analysis of the data. A.M.W. curated the data. J.S.F., M.C.T., N.K.S., E.N., M.K. and S.I. administered the project, acquired funding, and supervised research. A.M.W., M.C.T. and J.S.F. wrote the manuscript. M.C.T., A.M.W., J.S.F., E.N., I.D.Y., B.A.B. and S.C. edited the manuscript.

Competing interests

The authors declare no competing interests.

Additional information

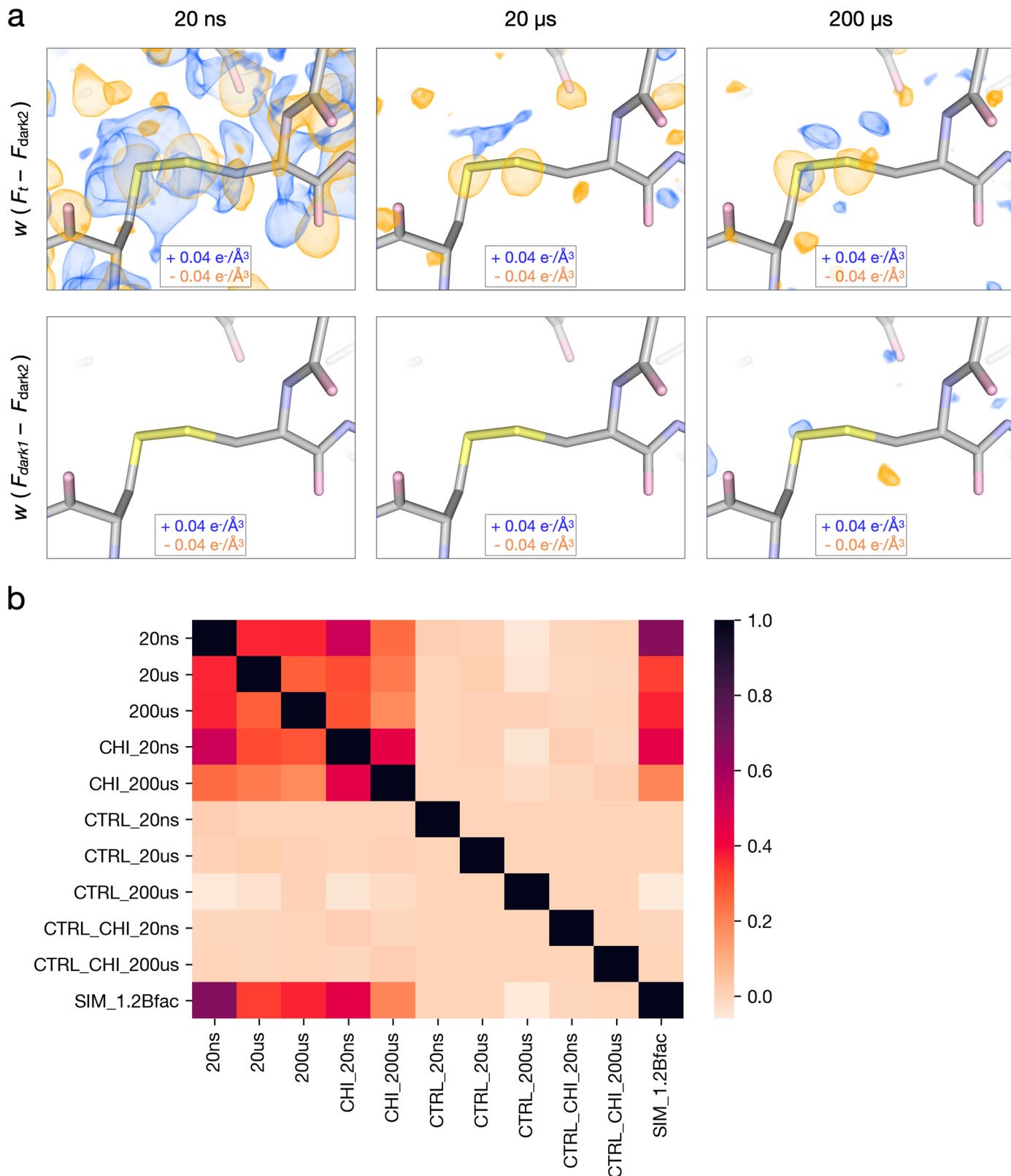
Extended data is available for this paper at <https://doi.org/10.1038/s41557-023-01329-4>.

Supplementary information The online version contains supplementary material available at <https://doi.org/10.1038/s41557-023-01329-4>.

Correspondence and requests for materials should be addressed to Eriko Nango or Michael C. Thompson.

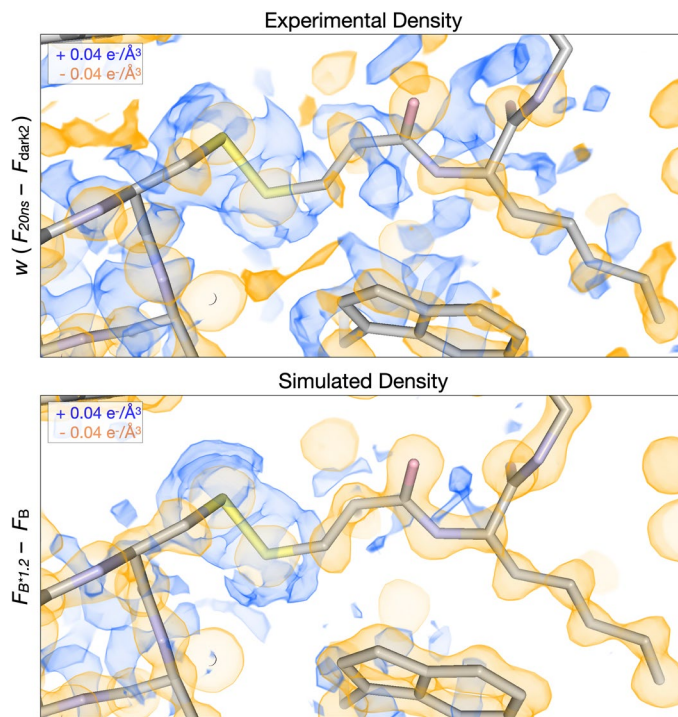
Peer review information *Nature Chemistry* thanks the anonymous reviewers for their contribution to the peer review of this work.

Reprints and permissions information is available at www.nature.com/reprints.



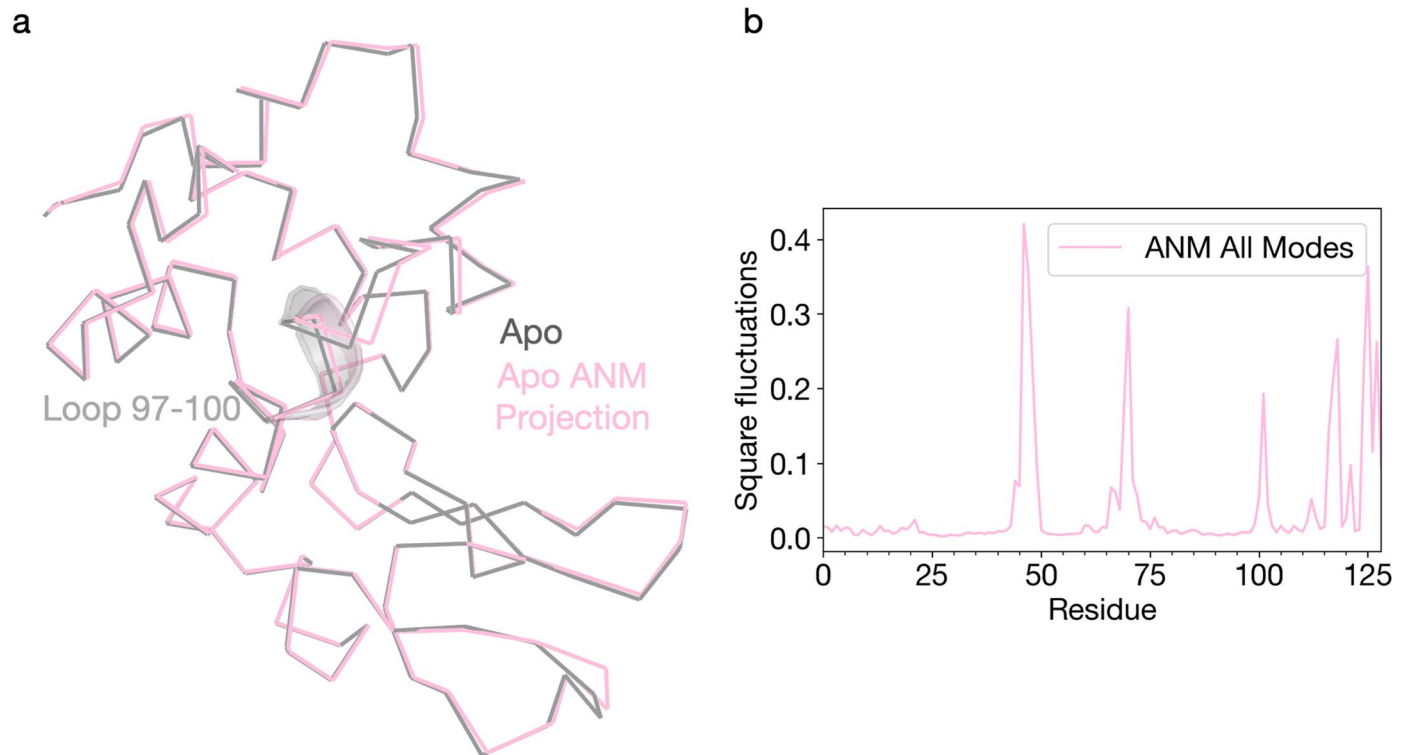
Extended Data Fig. 1 | Qualitative and quantitative assessment of time-resolved difference electron density features. (a) Comparison of weighted difference density maps for each pump-probe time delay ($F_{light} - F_{dark2}$) and matched controls ($F_{dark1} - F_{dark2}$) visualized at an absolute contour level of $\pm 0.04 \text{ e}^-/\text{\AA}^3$ alongside initial refined models. Atoms with greater electron density, such as the disulfide bridge between residues 76 and 94, display clear signals

across all experimental maps yet very little noise in matching controls. (b) Pairwise correlation coefficients were calculated between all difference maps, revealing varying levels of similarity between experimental maps and low noise across controls. Labels correspond to time-delay (20ns, 20 μ s, 200 μ s) presence of the inhibitor, chitobiose (CHI), whether a map was a matched control (CTRL), or based on simulated (SIM) structure factors (see Methods for details).



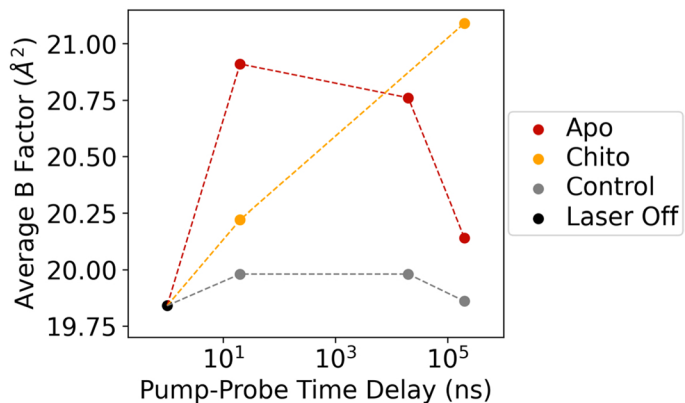
Extended Data Fig. 2 | Simulations of increased B-factors recapitulate signals present at the 20 ns pump-probe time delay. The experimental 20ns difference electron density map is visualized along with a simulated difference density map

created by linearly scaling the B-factors in the laser off structure by a factor of 1.2. Negative peaks (yellow) are centered upon atoms in both maps, surrounded by positive features (blue).



Extended Data Fig. 3 | Normal mode analysis of the Apo laser off structure. ProDy was used to generate an anisotropic network model based on the apo ground state conformation. (a) The apo structure was then visualized as a ribbon

diagram (grey) along with the same model projected along the combined ANM modes (green). (b) Per-residue RMSF values for the ANM model were plotted to quantify local dynamics.



Extended Data Fig. 4 | Effect of T-jump on average B-factor of refined apo and chitobiose-bound structures. Models were refined against Laser Off, Experiment (apo or chitobiose bound), or Control structure factors. Controls exhibit similar B-factors across all time points, while B-factors for experimental

measurements increase following T-jump. Apo models reveal a decline in B-factors at longer pump-probe time delays as complex motions develop, while chitobiose-bound experimental models retain higher B-factors at 200 μs , indicative of persistent, short-amplitude motions.

Extended Data Table 1 | Sample delivery and X-ray diffraction parameters for apo and chitobiose-bound data collection

Delivery Matrix	18% hydroxyethyl cellulose
Sample flow rate ($\mu\text{L}/\text{min}$)	2.5
Capillary diameter (μm)	75
Linear jet velocity (mm/s)	9.43
Pressure (psi)	\sim 3200
X-ray Source	SACLA - BL2
Photon Energy (keV)	10
X-ray pulse duration (fs)	\sim 10
Photons per pulse	\sim 1* 10^{11}
X-ray Repetition Rate (Hz)	30
IR Pump Laser Wavelength (nm)	1443
IR Pump Laser Energy (μJ)	540
IR Pump Laser Pulse Duration (ns)	7

Extended Data Table 2 | Crystallographic statistics for apo data collection^a

Dataset	Apo laser off	Light				Dark1			Dark2		
		Apo 20ns	Apo 20 us	Apo 200 us	Apo 20ns	Apo 20 us	Apo 200 us	Apo 20ns	Apo 20 us	Apo 200 us	Apo 200 us
Hit rate (%)	22.1	35.2	39.2	27.0	35.9	39.8	27.1	36.3	40.5	27.4	
Indexing rate (%)	84.7	91.7	87.8	82.8	87.9	87.0	81.6	88.1	87.2	81.3	
No. of images	9464	15253	13681	11931	14383	13559	11857	14454	13893	11950	
Resolution Range	28.09-1.57 (1.60-1.57)	31.62-1.57 (1.60-1.57)	28.11-1.57 (1.60-1.57)	28.11-1.57 (1.60-1.57)	28.09-1.57 (1.60-1.57)	28.09-1.57 (1.60-1.57)	28.09-1.65 (1.68-1.65)	28.09-1.57 (1.60-1.57)	28.09-1.57 (1.60-1.57)	28.09-1.57 (1.60-1.57)	28.09-1.57 (1.60-1.57)
Space Group	P4 ₃ 2 ₁ 2										
Unit-cell parameters											
a (Å)	79.45 +/- 0.10	79.52 +/- 0.13	79.52 +/- 0.10	79.51 +/- 0.11	79.44 +/- 0.10	79.44 +/- 0.09	79.45 +/- 0.10	79.44 +/- 0.09	79.44 +/- 0.09	79.46 +/- 0.11	
b (Å)	79.45 +/- 0.10	79.52 +/- 0.13	79.52 +/- 0.10	79.51 +/- 0.11	79.44 +/- 0.10	79.44 +/- 0.09	79.45 +/- 0.10	79.44 +/- 0.09	79.44 +/- 0.09	79.46 +/- 0.11	
c (Å)	38.16 +/- 0.07	38.23 +/- 0.08	38.21 +/- 0.05	38.19 +/- 0.05	38.19 +/- 0.06	38.20 +/- 0.05	38.19 +/- 0.06	38.19 +/- 0.06	38.20 +/- 0.06	38.19 +/- 0.06	
alpha (°)	90	90	90	90	90	90	90	90	90	90	
beta (°)	90	90	90	90	90	90	90	90	90	90	
gamma (°)	90	90	90	90	90	90	90	90	90	90	
Total Reflections	1593940 (39912)	3195992 (85262)	2208287 (56144)	1783773 (45477)	2279135 (58015)	2144941 (54395)	1601963 (48482)	2302697 (58593)	2202111 (55792)	1732358 (43260)	
Multiplicity	90.55 (46.63)	99.61	65.59	53.13	67.77	63.55	67.43	130.82 (68.45)	125.11 (65.18)	98.41 (50.54)	
Completeness (%)	99.97 (100)	(100.00)	(100.00)	(100.00)	99.97 (100)	99.97 (100)	99.97 (100)	99.97 (100)	99.97 (100)	99.98 (100)	
Mean I/sigma (I)	9.463 (5.889)	12.969 (6.918)	10.844 (6.633)	9.986 (6.280)	10.619 (6.240)	10.000 (6.040)	9.772 (6.896)	10.612 (6.120)	10.580 (6.353)	9.384 (6.167)	
Wilson B (Å)	14.1	15.37	15.38	15.1	15.23	15.30	14.807	15.26	15.38	14.84	
R-split (%)	9.4 (40.0)	5.9 (25.9)	7.5 (25.7)	8.5 (30.6)	7.8 (30.5)	8.4 (32.1)	9.9 (16.6)	8.1 (25.9)	7.9 (30.4)	9.2 (28.5)	
CC-int (%)	98.6 (17.0)	99.6 (34.6)	99.2 (44.5)	98.4 (37.7)	99.1 (39.7)	99.0 (31.9)	71.7 (81.9)	98.6 (56.0)	99.1 (55.0)	96.9 (44.3)	

^aStatistics for the highest-resolution shell are shown in parentheses.

Extended Data Table 3 | Refinement statistics for apo datasets^a

Dataset	Apo laser off	Light				Dark1				Dark2	
		Apo 20ns	Apo 20 us	Apo 200 us	Apo 20ns	Apo 20 us	Apo 200 us	Apo 20ns	Apo 20 us	Apo 200 us	Apo 200 us
PDB ID	8CW8	8CVU	8CW0	8CW5	8CVV	8CW1	8CW6	8CVW	8CW3	8CW7	
Resolution Range	28.09-1.57 (1.60-1.57)	31.62-1.57 (1.60-1.57)	28.11-1.57 (1.60-1.57)	28.11-1.57 (1.60-1.57)	28.09-1.57 (1.60-1.57)	28.09-1.57 (1.60-1.57)	28.09-1.65 (1.68-1.65)	28.09-1.57 (1.60-1.57)	28.09-1.57 (1.60-1.57)	28.09-1.57 (1.60-1.57)	28.09-1.57 (1.60-1.57)
Reflections used in refinement	17602 (1720)	17684 (1740)	17669 (1739)	17656 (1734)		17618 (1728)	17626 (1727)	15234 (1474)	17620 (1727)	17626 (1727)	17630 (1736)
Reflections used for R-free	895 (91)	902 (96)	898 (93)	899 (93)	896 (91)	896 (91)	776 (64)	896 (92)	896 (92)	896 (92)	
R-work	0.1462 (0.2973)	0.1511 (0.2744)	0.1448 (0.2476)	0.1527 (0.2791)	0.1449 (0.2178)	0.1478 (0.2228)	0.1364 (0.1727)	0.1463 (0.2134)	0.1440 (0.2152)	0.1525 (0.2531)	
R-free	0.1830 (0.3671)	0.1726 (0.3492)	0.1660 (0.3136)	0.1807 (0.3729)	0.1699 (0.2957)	0.1680 (0.2819)	0.1706 (0.2776)	0.1672 (0.2848)	0.1692 (0.2977)	0.1758 (0.3457)	
No. of non-H atoms	1209	1199	1203	1207	1204	1207	1203	1203	1198	1203	
macromolecules	1099	1099	1099	1099	1099	1099	1099	1099	1099	1099	
ligands	20	20	20	20	20	20	20	20	20	20	
solvent	96	86	90	94	91	94	90	90	85	90	
Protein residues	129	129	129	129	129	129	129	129	129	129	
RMS(bonds)	0.006	0.005	0.010	0.005	0.005	0.005	0.010	0.006	0.012	0.004	
RMS(angles)	0.80	0.69	0.91	0.79	0.79	0.77	0.95	0.82	0.99	0.69	
Ramachandran favored (%)	99.21	99.21	99.21	98.43	99.21	99.21	99.21	99.21	98.43	98.43	
Ramachandran allowed (%)	0.79	0.79	0.79	1.57	0.79	0.79	0.79	0.79	1.57	1.57	
Ramachandran outliers (%)	0.00	0.00	0.00	0.00	0.00	0.00	0.00	0.00	0.00	0.00	
Rotamer outliers (%)	2.56	2.56	2.56	2.56	2.56	2.56	2.56	2.56	2.56	2.56	
Clashscore	4.54	2.72	5.44	4.99	3.18	4.99	4.54	4.54	4.54	4.08	
Average B-factor	20.07	20.55	20.29	20.14	19.97	20.09	19.96	19.77	19.83	19.36	
macromolecules	18.58	19.25	18.88	18.73	18.60	18.65	18.61	18.43	18.53	18.03	
ligands	48.63	50.26	50.54	47.99	48.28	49.38	45.42	46.05	49.70	49.60	
solvent	33.01	32.28	32.73	32.54	32.23	32.57	32.41	32.00	31.71	30.89	

^aStatistics for the highest-resolution shell are shown in parentheses.

Extended Data Table 4 | Crystallographic statistics for chitobiose-bound data collection^a

Dataset	Chito laser off	Light		Dark1		Dark2	
		Chito 20ns	Chito 200us	Chito 20ns	Chito 200us	Chito 20ns	Chito 200us
Hit rate (%)	25.3	30.2	32.3	32.0	32.7	32.2	32.9
Indexing rate (%)	89.3	92.4	93.7	91.1	92.9	90.7	93.0
No. of images	31575	22549	21472	22489	20882	21715	21067
Resolution Range	30.74 -1.51 (1.54-1.51)	30.74 -1.48 (1.51-1.48)	30.74-1.50 (1.53-1.50)	30.74 -1.48 (1.51-1.48)	30.74-1.50 (1.53-1.50)	30.74 -1.48 (1.51-1.48)	30.74-1.50 (1.53-1.50)
Space Group	P4 ₃ 2 ₁ 2						
Unit-cell parameters							
a (Å)	78.55 +/- 0.22	79.05 +/- 0.16	78.98 +/- 0.12	78.91 +/- 0.11	78.85 +/- 0.09	78.91 +/- 0.11	78.85 +/- 0.09
b (Å)	78.55 +/- 0.22	79.05 +/- 0.16	78.98 +/- 0.12	78.91 +/- 0.11	78.85 +/- 0.09	78.91 +/- 0.11	78.85 +/- 0.09
c (Å)	38.30 +/- 0.13	38.50 +/- 0.05	38.47 +/- 0.04	38.48 +/- 0.05	38.51 +/- 0.04	38.48 +/- 0.05	38.51 +/- 0.04
alpha (°)	90	90	90	90	90	90	90
beta (°)	90	90	90	90	90	90	90
gamma (°)	90	90	90	90	90	90	90
Total Reflections	10094940 (25562)	3815383 (30777)	3053934 (31769)	3283906 (33942)	2892458 (34076)	3127348 (31601)	2895230 (33351)
Multiplicity	556.53 (28.92)	198.25 (32.95)	165.09 (35.54)	170.64 (36.34)	156.36 (38.12)	162.50 (33.83)	156.51 (37.31)
Completeness (%)	99.98 (100)	99.98 (100)	99.98 (100)	99.98 (100)	99.98 (100)	99.98 (100)	99.98 (100)
Mean I/sigma (I)	18.535 (3.367)	12.251 (3.347)	11.487 (3.673)	11.746 (3.977)	11.275 (3.834)	11.287 (3.831)	11.342 (3.883)
Wilson B (Å ²)	14.51	16.16	16.40	15.03	15.82	14.97	15.76
R-split (%)	3.5 (23.1)	5.5 (30.7)	5.7 (25.8)	6.1 (25.6)	6.1 (25.4)	6.2 (25.0)	6.2 (25.0)
CC-int (%)	99.9 (89.3)	99.6 (78.7)	99.5 (86.7)	99.3 (84.1)	99.4 (83.5)	99.4 (82.3)	99.4 (86.0)

^aStatistics for the highest-resolution shell are shown in parentheses.

Extended Data Table 5 | Refinement statistics for chitobiose-bound datasets^a

Dataset	Chito laser off	Light		Dark1		Dark2	
		Chito 20ns	Chito 200us	Chito 20ns	Chito 200us	Chito 20ns	Chito 200us
PDB ID	8CWB	8CWC	8CWF	8CWD	8CWG	8CWE	8CWH
Resolution Range	30.74-1.51 (1.54-1.51)	30.74-1.48 (1.51-1.48)	30.74-1.50 (1.53-1.50)	30.74-1.48 (1.51-1.48)	30.74-1.50 (1.53-1.50)	30.74-1.48 (1.51-1.48)	30.74-1.50 (1.53-1.50)
Reflections used in refinement	18138 (1754)	19245 (1873)	18499 (1825)	19245 (1873)	18499 (1825)	19245 (1873)	18499 (1825)
Reflections used for R-free	930 (97)	984 (103)	950 (99)	984 (103)	950 (99)	984 (103)	950 (99)
R-work	0.1357 (0.1329)	0.1316 (0.1246)	0.1332 (0.1105)	0.1306 (0.1147)	0.1292 (0.1066)	0.1298 (0.1137)	0.1321 (0.1051)
R-free	0.1679 (0.2134)	0.1683 (0.2273)	0.1660 (0.2130)	0.1633 (0.2039)	0.1663 (0.2210)	0.1632 (0.2090)	0.1679 (0.1996)
No. of non-H atoms	1157	1155	1153	1162	1160	1161	1166
macromolecules	1030	1030	1030	1030	1030	1030	1030
ligands	64	64	64	64	64	64	64
solvent	91	89	87	96	94	95	100
Protein residues	129	129	129	129	129	129	129
RMS(bonds)	0.018	0.016	0.019	0.018	0.018	0.019	0.020
RMS(angles)	1.21	1.19	1.20	1.19	1.17	1.23	1.21
Ramachandran favored (%)	99.21	99.21	99.21	99.21	99.21	99.21	99.21
Ramachandran allowed (%)	0.79	0.79	0.79	0.79	0.79	0.79	0.79
Ramachandran outliers (%)	0.00	0.00	0.00	0.00	0.00	0.00	0.00
Rotamer outliers (%)	0.00	0.00	0.92	0.92	0.92	0.00	0.92
Clashscore	3.87	5.80	5.32	3.87	5.80	3.38	5.80
Average B-factor	19.58	21.08	20.97	19.42	20.67	19.57	20.39
macromolecules	18.53	19.98	19.87	18.19	19.59	18.30	19.05
ligands	22.63	26.70	26.06	24.83	24.94	25.34	25.04
solvent	30.23	31.55	31.91	30.55	30.90	31.21	32.55

^aStatistics for the highest-resolution shell are shown in parentheses.

Michael C. Thompson

Corresponding author(s): Eriko Nango

Last updated by author(s): Jul 21, 2023

Reporting Summary

Nature Portfolio wishes to improve the reproducibility of the work that we publish. This form provides structure for consistency and transparency in reporting. For further information on Nature Portfolio policies, see our [Editorial Policies](#) and the [Editorial Policy Checklist](#).

Statistics

For all statistical analyses, confirm that the following items are present in the figure legend, table legend, main text, or Methods section.

n/a Confirmed

- The exact sample size (n) for each experimental group/condition, given as a discrete number and unit of measurement
- A statement on whether measurements were taken from distinct samples or whether the same sample was measured repeatedly
- The statistical test(s) used AND whether they are one- or two-sided
Only common tests should be described solely by name; describe more complex techniques in the Methods section.
- A description of all covariates tested
- A description of any assumptions or corrections, such as tests of normality and adjustment for multiple comparisons
- A full description of the statistical parameters including central tendency (e.g. means) or other basic estimates (e.g. regression coefficient) AND variation (e.g. standard deviation) or associated estimates of uncertainty (e.g. confidence intervals)
- For null hypothesis testing, the test statistic (e.g. F , t , r) with confidence intervals, effect sizes, degrees of freedom and P value noted
Give P values as exact values whenever suitable.
- For Bayesian analysis, information on the choice of priors and Markov chain Monte Carlo settings
- For hierarchical and complex designs, identification of the appropriate level for tests and full reporting of outcomes
- Estimates of effect sizes (e.g. Cohen's d , Pearson's r), indicating how they were calculated

Our web collection on [statistics for biologists](#) contains articles on many of the points above.

Software and code

Policy information about [availability of computer code](#)

Data collection	Data were collected using custom beamline control software developed at SACLA (Joti, et al. 2015).
Data analysis	Real time data analysis was performed using a pipeline (Nakane, et al. 2016) that calls upon Cheetah (Barty, et al. 2014) for hit finding, and CrystFEL (White, et al. 2012) for indexing and integration. Offline data analysis was performed using cctbx.xfel and cxi.merge for indexing, integration, and merging of the diffraction data (see references, no version numbers available). Structure determination by molecular replacement and refinement was performed using the PHENIX suite (v1.19.2_4158). Additional analysis of electron density and atomic models was performed using custom Python code that is publicly available on our GitHub page (see code availability statement). Code was implemented using Python 3 (v3.8.15), and the following libraries were used: numpy v1.19.2, scipy v1.5.2, pandas v1.1.5, matplotlib v3.3.2, seaborn v0.11.1, gemmi v0.4.5, prody v2.3.1, reciprocalspaceship v0.9.5.

For manuscripts utilizing custom algorithms or software that are central to the research but not yet described in published literature, software must be made available to editors and reviewers. We strongly encourage code deposition in a community repository (e.g. GitHub). See the Nature Portfolio [guidelines for submitting code & software](#) for further information.

Data

Policy information about [availability of data](#)

All manuscripts must include a [data availability statement](#). This statement should provide the following information, where applicable:

- Accession codes, unique identifiers, or web links for publicly available datasets
- A description of any restrictions on data availability
- For clinical datasets or third party data, please ensure that the statement adheres to our [policy](#)

Crystallographic models (refined against the raw structure factors as described above) and the associated reflection data have been deposited in the Protein Data Bank (PDB) under the following accession codes: 8CVU, 8CVV, 8CVW, 8CW0, 8CW1, 8CW3, 8CW5, 8CW6, 8CW7, 8CW8, 8CWB, 8CWC, 8CWD, 8CWE, 8CWF, 8CWG, 8CWH. The model used for MR is also available from the PDB under accession code 1IEE. Additionally, the raw data are publicly available at CXIDB under ID205.

Human research participants

Policy information about [studies involving human research participants and Sex and Gender in Research](#).

Reporting on sex and gender

N/A

Population characteristics

N/A

Recruitment

N/A

Ethics oversight

N/A

Note that full information on the approval of the study protocol must also be provided in the manuscript.

Field-specific reporting

Please select the one below that is the best fit for your research. If you are not sure, read the appropriate sections before making your selection.

Life sciences

Behavioural & social sciences

Ecological, evolutionary & environmental sciences

For a reference copy of the document with all sections, see nature.com/documents/nr-reporting-summary-flat.pdf

Life sciences study design

All studies must disclose on these points even when the disclosure is negative.

Sample size

The number of crystals used to obtain each data set was determined using real time data analysis. Knowing that in serial crystallography, accurate intensity estimation from partial reflections relies on high multiplicity, and that the multiplicity of the merged data tends to decrease as a function of resolution, we continued collecting data until we reached a data multiplicity of >10 for the highest resolution reflections. This threshold was selected, somewhat arbitrarily, based on our team's previous experience processing serial crystallography data. Subsequent data analysis and calculation of CC_{1/2} and I/σ(I) quality metrics led to a reduction in the maximum resolution of the data, resulting in an even higher multiplicity for unique reflection measurements from the same number of crystal specimens.

Data exclusions

Diffraction images that could not be fit to the indexed lattice model were discarded.

Replication

Data sets arise from >10,000 individual pump-probe measurements, with controls to remove the effect of covariates (see below). Limited XFEL beamtime precludes the collection of identical data sets for comparison, but the CC_{1/2} and R-split values reported represent comparisons of random-half datasets.

Randomization

Samples cannot be randomized (i.e. consecutive measurements necessarily come from the same sample batch), therefore we collected interleaved control measurements to remove the effect of systematic, batch-to-batch variation of samples.

Blinding

Sample blinding is not a standard practice in structural biology.

Reporting for specific materials, systems and methods

We require information from authors about some types of materials, experimental systems and methods used in many studies. Here, indicate whether each material, system or method listed is relevant to your study. If you are not sure if a list item applies to your research, read the appropriate section before selecting a response.

Materials & experimental systems

n/a	Involved in the study
<input checked="" type="checkbox"/>	Antibodies
<input checked="" type="checkbox"/>	Eukaryotic cell lines
<input checked="" type="checkbox"/>	Palaeontology and archaeology
<input checked="" type="checkbox"/>	Animals and other organisms
<input checked="" type="checkbox"/>	Clinical data
<input checked="" type="checkbox"/>	Dual use research of concern

Methods

n/a	Involved in the study
<input checked="" type="checkbox"/>	ChIP-seq
<input checked="" type="checkbox"/>	Flow cytometry
<input checked="" type="checkbox"/>	MRI-based neuroimaging